



# Nighttime and Daytime Dark Oxidation Chemistry in Wildfire Plumes: An Observation and Model Analysis of FIREX-AQ Aircraft Data

5 Zachary C.J. Decker<sup>1,2,3</sup>, Michael A. Robinson<sup>1,2,3</sup>, Kelley C. Barsanti<sup>4</sup>, Ilann Bourgeois<sup>1,2</sup>, Matthew M. Coggon<sup>1,2</sup>, Joshua P. DiGangi<sup>5</sup>, Glenn S. Diskin<sup>5</sup>, Frank M. Flocke<sup>6</sup>, Alessandro Franchin<sup>1,2,6</sup>, Carley D. Fredrickson<sup>7</sup>, Samuel R. Hall<sup>6</sup>, Hannah Halliday<sup>5,\*</sup>, Christopher D. Holmes<sup>8</sup>, L. Gregory Huey<sup>9</sup>, Young Ro Lee<sup>9</sup>, Jakob Lindaas<sup>10</sup>, Ann M. Middlebrook<sup>1</sup>, Denise D. Montzka<sup>6</sup>, Richard Moore<sup>11</sup>, J. Andrew Neuman<sup>1,2</sup>, John B. Nowak<sup>11</sup>, Brett B. Palm<sup>7</sup>, Jeff Peischl<sup>1,2</sup>, Pamela S. Rickly<sup>1,2</sup>, Andrew W. Rollins<sup>1</sup>,  
10 Thomas B. Ryerson<sup>1</sup>, Rebecca H. Schwantes<sup>1,2</sup>, Lee Thornhill<sup>5,11</sup>, Joel A. Thornton<sup>7</sup>, Geoffrey S. Tyndall<sup>6</sup>, Kirk Ullmann<sup>6</sup>, Paul Van Rooy<sup>4</sup>, Patrick R. Veres<sup>1</sup>, Andrew J. Weinheimer<sup>6</sup>, Elizabeth Wiggins<sup>5,12</sup>, Edward Winstead<sup>5,11</sup>, Caroline Womack<sup>1,2</sup>, Steven S. Brown<sup>1,3</sup>

<sup>1</sup>NOAA Chemical Sciences Laboratory (CSL), Boulder, Colorado 80305, USA

15 <sup>2</sup>Cooperative Institute for Research in Environmental Sciences, University of Colorado Boulder, Boulder, Colorado 80309, USA

<sup>3</sup>Department of Chemistry, University of Colorado Boulder, Boulder, Colorado 80309-0215, USA

<sup>4</sup>Department of Chemical and Environmental Engineering and College of Engineering – Center for Environmental Research and Technology (CE-CERT), University of California, Riverside, Riverside, CA 92507, USA

<sup>5</sup>NASA Langley Research Center, MS 483, Hampton, VA 23681, USA

20 <sup>6</sup>Atmospheric Chemistry Observations and Modeling Laboratory, National Center for Atmospheric Research, Boulder, CO 80301, USA

<sup>7</sup>Department of Atmospheric Sciences, University of Washington, Seattle, WA 98195, USA

<sup>8</sup>Department of Earth, Ocean, and Atmospheric Science, Florida State University, Tallahassee, FL, 32304, USA

<sup>9</sup>School of Earth and Atmospheric Sciences, Georgia Institute of Technology, Atlanta, GA 30332, USA

25 <sup>10</sup>Colorado State University, Department of Atmospheric Science, Fort Collins, CO, USA

<sup>11</sup>Science Systems and Applications, Inc. (SSAI), Hampton, VA, USA

<sup>12</sup>Universities Space Research Association, Columbia, MD, USA

\* Now at EPA Office of Research and Development, RTP, NC 27711, USA

30 *Correspondence to:* Steven S. Brown (steven.s.brown@noaa.gov)  
**Abstract.**

Wildfires are increasing in size across the western U.S., leading to increases in human smoke exposure and associated negative health impacts. The impact of biomass burning (BB) smoke, including wildfires, on regional air quality depends on emissions,  
35 transport, and chemistry, including oxidation of emitted BB volatile organic compounds (BBVOCs) by the hydroxyl radical (OH), nitrate radical (NO<sub>3</sub>), and ozone (O<sub>3</sub>). During the daytime, when light penetrates the plumes, BBVOCs are oxidized mainly by O<sub>3</sub> and OH. In contrast, at night, or in optically dense plumes, BBVOCs are oxidized mainly by O<sub>3</sub> and NO<sub>3</sub>. This work focuses on the transition between daytime and nighttime oxidation, which has significant implications for the formation of secondary pollutants and loss of nitrogen oxides (NO<sub>x</sub> = NO + NO<sub>2</sub>), and has been understudied. We present wildfire plume  
40 observations made during FIREX-AQ (Fire Influence on Regional to Global Environments and Air Quality), a field campaign



involving multiple aircraft, ground, satellite, and mobile platforms that took place in the United States in the summer of 2019 to study both wildfire and agricultural burning emissions and atmospheric chemistry. We use observations from two research aircraft, the NASA DC-8 and the NOAA Twin Otter, with a detailed chemical box model, including updated phenolic mechanisms, to analyze smoke sampled during mid-day, sunset, and nighttime. Aircraft observations suggest a range of NO<sub>3</sub> production rates (0.1 – 1.5 ppbv h<sup>-1</sup>) in plumes transported both mid-day and after dark. Modeled initial instantaneous reactivity toward BBVOCs for NO<sub>3</sub>, OH, and O<sub>3</sub> is 80.1 %, 87.7 %, 99.6 %, respectively. Initial NO<sub>3</sub> reactivity is 10 – 10<sup>4</sup> times greater than typical values in forested or urban environments and reactions with BBVOCs account for ≥ 98 % of NO<sub>3</sub> loss in sunlit plumes (jNO<sub>2</sub> up to 4×10<sup>-3</sup> s<sup>-1</sup>), while conventional photochemical NO<sub>3</sub> loss through reaction with NO and photolysis are minor pathways. Alkenes and furans are mostly oxidized by OH and O<sub>3</sub> (11 – 43%, 54 – 88% for alkenes; 18 – 55 %, 39 – 76 %, for furans, respectively), but phenolic oxidation is split between NO<sub>3</sub>, O<sub>3</sub>, and OH (26 – 52 %, 22 – 43 %, 16 – 33 %, respectively). Nitrate radical oxidation accounts for 26 – 52 % of phenolic chemical loss in sunset plumes and in an optically thick plume. Nitrocatechol yields varied between 33 % and 45 %, and NO<sub>3</sub> chemistry in BB plumes emitted late in the day is responsible for 72 – 92 % (84 % in an optically thick mid-day plume) of nitrocatechol formation and controls nitrophenolic formation overall. As a result, overnight nitrophenolic formation pathways account for 56 ± 2 % of NO<sub>x</sub> loss by sunrise the following day. In all but one overnight plume we model, there is remaining NO<sub>x</sub> (13 % – 57 %) and BBVOCs (8 % – 72 %) at sunrise.

## 1 Introduction

It is well known that biomass burning (BB), including wildfires, can have large impacts on air quality at local, regional and global scales (Jaffe et al., 2020). The relative impact and importance of wildfire smoke on air quality in the western U.S. is increasing with decreasing anthropogenic volatile organic compound (VOC) and nitrogen oxide (NO<sub>x</sub> = NO + NO<sub>2</sub>) emissions (Bishop and Haugen, 2018; Silvern et al., 2019; Warneke et al., 2012; Xing et al., 2015). This increase is compounded by growing wildfire emissions caused by anthropogenic influences such as human-caused climate change and past wildland management practices. Twentieth century suppression of western U.S. wildfires has led to increased fuel loadings and thus fire potential (Higuera et al., 2015; Marlon et al., 2012; Parks et al., 2015). A warmer and drier climate in the western U.S. resulting from human-caused climate change has exacerbated fire potential and has resulted in an increase in the frequency of large wildfires since the 1980s (Abatzoglou and Williams, 2016; Balch et al., 2017; Barbero et al., 2015; Dennison et al., 2014; Marlon et al., 2012; Westerling et al., 2006; Westerling, 2016; Williams et al., 2019).

Wildfires emit NO<sub>x</sub>, nitrous acid (HONO), biomass burning VOCs (BBVOCs) and particulate matter (PM) that evolve chemically on a range of time scales, from seconds to weeks downwind (Akagi et al., 2011; Andreae and Merlet, 2001; Decker et al., 2019; Hatch et al., 2015, 2017; Koss et al., 2018; Palm et al., 2020). These emissions and their chemical products influence air quality through ozone (O<sub>3</sub>) production, emitted PM, and secondary organic aerosol formation (SOA) (Brey et al., 2018; Jaffe et al., 2020; Jaffe and Wigder, 2012; Lu et al., 2016; Palm et al., 2020; Phuleria et al., 2005). However, the evolution



of the smoke downwind is influenced by several variables such as fuel type, burn conditions, moisture content, nitrogen content, meteorology, and time of day.

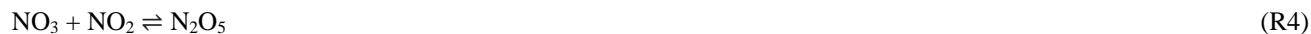
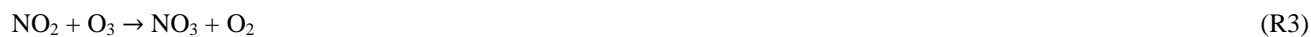
75 Like most atmospheric oxidation processes, the oxidation of BBVOCs is influenced by three key atmospheric oxidants: O<sub>3</sub>, the hydroxyl radical (OH), and the nitrate radical (NO<sub>3</sub>). The amount of each oxidant present in a plume is influenced by emissions of NO<sub>x</sub>, plume mixing with background air, and the amount of sunlight that penetrates a plume. Photolysis of HONO can be an important source of HO<sub>x</sub> (= OH + HO<sub>2</sub>) in the first three hours of aging for wildfires sampled in the western U.S. (Peng et al., 2020). Further, atmospheric background levels of O<sub>3</sub>, as well as photochemical O<sub>3</sub> production within a smoke  
80 plume, can provide O<sub>3</sub> for plume oxidation (Jaffe and Wigder, 2012). However, there is limited understanding of the role of NO<sub>3</sub> oxidation in biomass burning plumes.

During daytime, NO<sub>3</sub> is rapidly destroyed by photolysis (R1), and in urban plumes it is destroyed even more rapidly by reaction with NO (R2, τ < 10 s) (Brown and Stutz, 2012; Wayne et al., 1991).



Therefore, although the role of NO<sub>3</sub> in nighttime BBVOC oxidation has been considered previously, the role of NO<sub>3</sub> as a daytime oxidant has been neglected (Decker et al., 2019; Keywood et al., 2015; Kodros et al., 2020; Palm et al., 2020).

Despite the potential for rapid loss of NO<sub>3</sub> with sunlight and NO, wildfire plumes provide a unique environment which promotes NO<sub>3</sub> chemistry. NO<sub>3</sub> is produced within a smoke plume by the gas-phase reaction of O<sub>3</sub> and NO<sub>2</sub> (R3) and is a  
90 precursor for N<sub>2</sub>O<sub>5</sub> (R4), a NO<sub>x</sub> reservoir (Brown and Stutz, 2012). N<sub>2</sub>O<sub>5</sub> may undergo heterogeneous uptake to form ClNO<sub>2</sub> and HNO<sub>3</sub> according to the branching ratio φ (R5) (Chang et al., 2011; McDuffie et al., 2018). NO<sub>3</sub> can also be directly taken up by aerosol (R6) or react with BBVOCs (R7).



Modeled NO<sub>3</sub> reactivity was found to be mostly (>99 %) from reactions with BBVOCs (R7) as opposed to heterogeneous reactions with aerosol particles (R5 – 6) in an agricultural burning plume sampled after sunset (Decker et al., 2019). This is  
100 the result of elevated concentrations of several highly reactive BBVOCs within the plume. Specifically, directly emitted aromatic alcohols (phenolics) react with NO<sub>3</sub> at near the gas-kinetic limit to form nitrophenolics, a subset of nitroaromatics, and secondary organic aerosol (Finewax et al., 2018; Lauraguais et al., 2014; Liu et al., 2019; Xie et al., 2017). Nitrophenolics absorb strongly in the ultraviolet and visible regions of the solar spectrum, and are expected to significantly contribute to BrC absorption (Palm et al., 2020; Selimovic et al., 2020). Phenolic reactions with OH in the presence of NO<sub>x</sub> also form  
105 nitrophenolics, but at one third the yield (Finewax et al., 2018).



Wildfire emissions typically peak in the mid-afternoon to evening, and continue to emit smoke into the night (Giglio, 2007; Li et al., 2019). Furthermore, large smoke plumes can be optically thick, with little photolysis at their center. This means that most smoke plumes will be oxidized in the dark during some, if not all, of their transport. Yet, the vast majority of in-situ field investigations of biomass burning smoke has been conducted under sunlight, and most analyses of daytime smoke plumes have so far focused on plume oxidation by OH and O<sub>3</sub> only (Coggon et al., 2019; Keywood et al., 2015; Liu et al., 2016; Palm et al., 2020).

In the summer of 2019, both the NOAA Twin Otter and the NASA DC-8 aircraft executed a series of research flights sampling smoke plumes as part of the Fire Influence on Regional to Global Environments and Air Quality (FIREX-AQ) campaign. Here, we present a detailed analysis of smoke plumes from three fires using observations from FIREX-AQ to constrain a detailed zero-dimensional (0-D) chemical box model. We investigate one optically-thick plume emitted mid-day, three smoke plumes emitted near or at sunset, and one theoretical plume emitted after sunset. We discuss the reactivity and competitive oxidation for all oxidants, NO<sub>3</sub>, O<sub>3</sub>, and OH, toward a suite of BBVOCs. Further, we detail the oxidation pathways of phenolics, discuss the variables that affect the yield of nitrophenolics, and describe how nitrophenolics have a significant impact on NO<sub>x</sub> loss and fate.

## 2 Methods

### 2.1 Aircraft Measurements

FIREX-AQ was a large-scale multi-platform campaign that took place during the summer of 2019 in the United States to study both wildfire and agricultural burning smoke. Both the NOAA Twin Otter and the NASA DC-8 aircraft executed a series of research flights sampling smoke plumes as part of this campaign. A main science goal of the NOAA Twin Otter was to investigate nighttime plume chemistry. However, due to a less active fire season in 2019 (NIFC, 2019) and to the decreasing smoke injection height with time of day for the sampled fires, smoke emitted after dark proved difficult to sample reliably within the altitude range of the NOAA Twin Otter. While the NOAA Twin Otter sampled over a dozen plumes after sunset, plume age estimates (described below) suggest these plumes were emitted before or at sunset. The NASA DC-8 aircraft sampled large, optically thick, plumes both mid-day and near sunset. In the following sections we briefly describe the instrumentation used for this analysis, which are listed in SI Table 1. More information and data can be found at <https://csl.noaa.gov/projects/firex-aq/twinotterCHEM/>, <https://espo.nasa.gov/firex-aq>, and <https://www-air.larc.nasa.gov/missions/firex-aq/index.html>.

#### 2.1.1 NOAA Twin Otter Instrument Descriptions

The NOAA Twin Otter sampled nine wildfires with 39 flights between 3 August 2019 and 5 September 2019 in the western U.S. The aircraft was based mainly in Boise, ID and briefly in Cedar City, UT. The NOAA Twin Otter payload limited flight duration to 3.0 h or less and the aircraft typically flew 2 – 3 times in a day to achieve plume sampling from mid-afternoon into



the night. Aircraft speed was  $71.8 \pm 3.8 \text{ m s}^{-1}$  (average  $\pm 1-\sigma$ ), which yields a horizontal resolution of  $\sim 70 \text{ m}$  for the in situ 1 s measurements. Attempts to probe the same air mass downwind, known as Lagrangian sampling, proved difficult to achieve due to complex plume structure, terrain and airspace. Therefore, we define the sampling strategy as semi-Lagrangian.

140 This analysis uses NOAA Twin Otter observations of BBVOCs and HONO from a University of Washington Iodide High Resolution Time of Flight Chemical Ionization Mass Spectrometer (UW I<sup>-</sup> HR ToF CIMS, 2 Hz, Lee et al., 2014) as well as a Tenax cartridge sampler with subsequent GCxGC analysis for speciated BBVOCs (intermittent transect integrations, Hatch et al., 2015; Mondello et al., 2008), which we use to support mass assignments from the UW I<sup>-</sup> HR ToF CIMS for some phenolic compounds (see SI).

145 We use data from a commercial cavity ringdown spectrometer (Picarro G2401-m) for measurements of CO, CO<sub>2</sub>, and CH<sub>4</sub> (0.5 Hz, Crosson, 2008). We use measurements from a custom chemiluminescence instrument (1 Hz) for NO, NO<sub>2</sub> and O<sub>3</sub> (Sparks et al., 2019). Aerosol surface area measurements were collected by an ultra-high sensitivity aerosol spectrometer (UHSAS, 1 Hz, Kupc et al., 2018). The aircraft had a standard meteorological probe (Aventech ARIM 200) for temperature, pressure, relative humidity, wind speed and direction. We use NO<sub>2</sub> photolysis rates ( $j_{\text{NO}_2}$ ) collected by upward and downward

150 facing  $j_{\text{NO}_2}$  filter radiometers (Metcon, GmbH, 1 Hz, Kupc et al., 2018; Warneke et al., 2016).

### 2.1.2 NASA DC-8 Instrument Descriptions

The NASA DC-8 aircraft sampled 14 wildfires in the western U.S. while based in Boise, ID as well as about 90 prescribed agricultural southeastern U.S. fires while based in Salina, KS between 22 July 2019 and 5 September 2019. Aircraft speed was  $325 \pm 6.6 \text{ m s}^{-1}$ , which yields a horizontal resolution of  $\sim 325 \text{ m}$  for the in situ 1 s measurements. Similar to the NOAA Twin

155 Otter, sampling was semi-Lagrangian.

In this analysis we use measurements of CO from a tunable diode laser spectrometer (1 Hz, Sachse et al., 1991) when available and from a cavity enhanced spectrometer (CES, 1 Hz, Eilerman et al., 2016) when unavailable. In the fires investigated here both instruments agree well within  $<1 \%$ . Measurements of NO<sub>2</sub>, NO<sub>y</sub> and O<sub>3</sub> are provided by a NOAA chemiluminescence (CL, 1 Hz, Pollack et al., 2010; Ridley et al., 1992; Stedman et al., 1972) instrument. When measurements of NO<sub>2</sub> by the

160 NOAA CL instrument are unavailable we use measurements by a NOAA CES (1 Hz, Min et al., 2016). These two measurement methods of NO<sub>2</sub> agree within 12 % for the fires we investigate. We use measurements of NO by a laser induced fluorescence instrument (1 Hz, Rollins et al., 2020). Measurements of BBVOCs and HONO are taken from the NOAA I<sup>-</sup> ToF CIMS (1 Hz, Neuman et al., 2016; Veres et al., 2020). PAN measurements were performed by a thermal dissociation CIMS (1 Hz, Ro Lee et al., 2020). Aerosol surface area measurements are taken from a scanning mobility particle sizer and laser aerosol

165 spectrometer (SMPS and LAS, 1 Hz, LAS, n.d.; Moore et al., 2021; SMPS, n.d.). Spectrally resolved actinic flux was measured with separate upward and downward facing actinic flux optics (CAFS, 1 Hz, Shetter and Müller, 1999). These fluxes were used to calculate photolysis rates using the photochemistry routine contained in the NCAR TUV model (v5.3.2).



### 2.1.3 Plume Age Determination

170 Plume age estimates are made by air parcel trajectories computed in the HYSPLIT trajectory model with multiple high-resolution meteorological datasets (HRRR 3 km, NAM CONUS nest 3 km, and GFS 0.25°). These estimates account for buoyant plume rise as well as horizontal advection. Uncertainties in plume age are determined from spread between the meteorological datasets, mismatch between observed and archived winds, and trajectory spatial error in missing the known fire source. Typical uncertainties are 25 % of the estimated age (Holmes et al., 2020).

### 2.2 Fire Descriptions

175 This analysis focuses on four semi-Lagrangian experiments from three separate fire complexes: the Castle fire plume in northern Arizona, the 204 Cow fire plume in central Oregon (referred to as Cow from here on), and two from the Williams Flats fire plume in eastern Washington (referred to as WF1 and WF2 from here on). Table 1 summarizes fire locations, sampling platform, sampling times, and fuel types (Inciweb, 2019b, 2019c, 2019a). Figure 1 displays flight paths. We select the above plume samplings among others because of their data coverage, potential for active chemistry and sunset-like conditions defined as the following: 1) sampled by semi-Lagrangian transects roughly perpendicular to the prevailing wind direction, 2) had available measurements of CO, NO<sub>x</sub>, HONO, O<sub>3</sub>, photolysis rates, and aerosol surface area, 3) contained either reduced plume-center photolysis ( $j\text{NO}_2 < 10^{-3} \text{ s}^{-1}$ ) or plume ages <3 h by sunset, and 4) sampled a plume age range >1 h. The WF fire started on 2 August 2019 and grew to a total of 44,446 acres before it was contained on 25 August 2019. The fuel was mostly short grass (1 ft tall) as well as ponderosa and mixed conifer timber (Inciweb, 2019c). The DC-8 aircraft performed 185 three semi-Lagrangian smoke transect patterns on 7 August 2019 when the fire had burned about 25,000 acres. This study focuses on the first two sampling patterns: the WF1 (Figure 1A) and WF2 (Figure 1B). WF1 contained smoke emitted from about 14:00 – 16:00 local time (PDT), or the early to late afternoon, while the second pattern sampled smoke emitted near sunset. The sampled smoke varied in age from 36 min – 4 h.

The Castle fire began on 12 July 2019 and was allowed to burn the mixed conifer fuel in a defined area that eventually reached 190 19,368 acres, and burned out on 15 October 2019 (Inciweb, 2019b). The Twin Otter aircraft performed one semi-Lagrangian transect pattern during sunset on 21 August 2019 when small pockets of remaining fuels were burning. The sampled smoke varied in age from approximately 2 min – 1.5 h. The Castle fire had a neighboring fire named Ikes. Smoke from the Ikes fire visually mixed (SI Figure 1) with the Castle fire plume after the fourth transect downwind of the Castle fire (Figure 1D). For that reason, this analysis focuses on the first four transects only.

195 The Cow fire started on 9 August 2019 and was allowed to burn eventually reaching 9,668 acres by 15 September 2019. The fuel was mainly lodgepole pine at lower elevations and mixed conifer at higher elevations with abundant downed timber. The Twin Otter aircraft performed three semi-Lagrangian transect patterns on 28 August 2019, by which time the fire had burned 3,441 acres (Inciweb, 2019a). This study focuses on the third semi-Lagrangian transect pattern, which was conducted after sunset. The sampled smoke in this analysis had aged approximately 2 – 3 h.



## 200 2.3 Box Model Description

We modeled smoke plumes from three fires (Castle, Cow, and WF). We present four model cases (Castle, Cow, WF1, WF2) constrained by aircraft observations and one case (Dark) identical to the WF2 case except all modeled photolysis frequencies are set to zero. The Dark case simulates oxidation of the WF2 plume if it was emitted after sunset. The Dark case is used to understand the effect of photolysis on the WF2 model run.

205 The Cow, WF2, and Dark cases are run from emission until sunrise the following day (about 12 h). The Castle case is run for 2.6 h until all BB emissions are near ( $\ll 1\%$ ) background levels. We run the WF1 case until the age of the oldest sampled smoke ( $\sim 4$  h) because we do not have any observations of photolysis rates with which to constrain the model past that point. Box modelling was performed using the Framework for 0-D Atmospheric Modelling (F0AM) (Wolfe et al., 2016) with chemistry and emissions described in the following section. We start the model at the emission time (age = 0) of the earliest  
210 smoke transect (the youngest sampled smoke), which occurred between 2 min and 2 h before the first plume transect, depending on the plume. In most cases, we use an iterative method constrained to a subset of observations (described in section 2.3.3) to estimate emissions.

While all plumes were sampled by aircraft following a semi-Lagrangian strategy, we model each plume as if it were Lagrangian - i.e., it is assumed that the emissions and fire conditions were constant over the course of sampling. Further, we constrain our  
215 model to plume-center observations because we model only the plume-center and represent mixing through a dilution term. Consequently, the model does not represent differences in chemical regimes that may occur between the center and edge of a plume.

### 2.3.1 Chemistry and Emissions

Our model uses the master chemical mechanism (MCM, v3.3.1 via <http://mcm.york.ac.uk>), in conjunction with a NOAA  
220 biomass burning mechanism included in F0AM v4.0 (Bloss et al., 2005; Coggon et al., 2019; Decker et al., 2019; Jenkin et al., 1997, 2003, 2012, 2015) and updates to OH- and NO<sub>3</sub>-initiated oxidation of phenolic compounds (Bolzacchini et al., 2001; Calvert et al., 2011; Finewax et al., 2018; Nakao et al., 2011; Olariu et al., 2002, 2013; Schwantes et al., 2017). Briefly, we update the phenol oxidation product yields of catechol, methylcatechol, and three dimethylcatechols reacting with NO<sub>3</sub> and OH. Further, we expand the phenolic oxidation pathways in the MCM from 50 to 140 reactions by extrapolating analogous  
225 branching ratios, rate coefficients and products from studies of phenol and cresol oxidation (see SI).

We initiate the model using an emissions inventory of 302 BBVOCs in the form of emission ratios (ERs).

$$ER_x = \frac{x \text{ (ppbv)}}{CO \text{ (ppmv)}}, \quad (1)$$

The ER inventory is described in detail in Decker et al., 2019 and uses an average of BBVOC emissions studies of ponderosa  
230 pine fuel from the Fire Lab at Missoula Experiment (FLAME-4) (Hatch et al., 2017) and the Fire Influence on Regional and Global Environments Experiment (FIREX lab) (Koss et al., 2018) with rate coefficients taken from literature when available



or estimated when unavailable. Approximately 250 BBVOCs in the inventory are not included in the MCM and do not have published mechanisms. Therefore, reactions of those compounds with  $\text{NO}_3$ , OH, and  $\text{O}_3$  lead to a generic product.

The model includes heterogeneous  $\text{NO}_3$  and  $\text{N}_2\text{O}_5$  uptake onto aerosol, calculated for  $\text{NO}_3$  heterogeneous reactivity, as

$$k_{\text{NO}_3}^{\text{aerosol}} = K_{\text{eq}}[\text{NO}_2]k_{\text{N}_2\text{O}_5} + k_{\text{NO}_3+\text{aerosol}} \quad (2)$$

235 where  $k_{\text{NO}_3}^{\text{aerosol}}$  is a first order rate coefficient,  $K_{\text{eq}}$  is the equilibrium rate constant for (R4) and  $k_{\text{NO}_3+\text{aerosol}}$  is a first order rate coefficient for uptake expressed below. Note, however, that the following equation applies for small uptake coefficients and small aerosol diameters where gas phase diffusion does not limit uptake.

$$k_{\text{x}+\text{aerosol}} = \frac{\gamma \bar{c} SA}{4} \quad (3)$$

240 Here  $\gamma$  is the aerosol uptake coefficient,  $\bar{c}$  is the mean molecular speed, and SA is the measured aerosol surface area at plume-center. We use  $\gamma_{\text{N}_2\text{O}_5} = 10^{-2}$  and  $\gamma_{\text{NO}_3} = 10^{-3}$  (McDuffie et al., 2018). Values for  $\gamma_{\text{NO}_3}$  can have a wide range; therefore we include calculations with  $\gamma_{\text{NO}_3} = 10^{-3} - 1$  as described in section 3.1 (Brown and Stutz, 2012).

### 2.3.2 Model Constraints

Our model is constrained to plume-center and, for some compounds, background measurements of aerosol surface area, photolysis rates,  $\text{O}_3$ , CO,  $\text{NO}_x$ , HONO, and total oxidized nitrogen ( $\text{NO}_y$ ). Measurements of  $\text{NO}_y$  are only available from the  
245 DC-8 measurements. We also constrain our models to the meteorological conditions pressure, temperature, and relative humidity. Fire emissions and photolysis conditions can change rapidly, therefore we constrain the model to a subset of plume transects. We chose transects that showed a monotonic decrease of CO with distance from the fire, cover an age range of at least one hour, and have similar emission times as shown in SI Figure 2 and SI Figure 3.

All model runs included a constant first-order plume dilution rate coefficient ( $k_{\text{dil}}$ ) determined by applying an exponential fit  
250 to observed CO as a function of plume age (SI Figure 3). We fit only points used to constrain the model and fixed the exponential fit offset to the observed CO background. We applied  $k_{\text{dil}}$  to all species in the model. We find values of  $k_{\text{dil}}$  that range between  $4.5 - 60 \times 10^{-5} \text{ s}^{-1}$  (SI Table 2), equivalent to a lifetime ( $\tau_{\text{dil}} = 1/k_{\text{dil}}$ ) of 0.5 – 6.2 h.

Plume-center observations were determined using a “top 5 %” method as described by Peng et al., 2020. Briefly, within a  
255 transect we determine the location of the greatest 5 % of observations for CO and use that location of the plume for analysis of other compounds. This method obtains an average observation for the center, or most concentrated, parts of the plume. Reported uncertainties are the  $1-\sigma$  variability of the top 5 % region and instrument uncertainties added in quadrature.

Particulate matter in BB plumes attenuates sunlight, and thus photolysis rates, in a process we refer to as plume darkening. In  
WF plumes we use plume-center observations of 20 photolysis rates (listed in SI Table 3), but for the Castle and Cow plumes only  $\text{jNO}_2$  is available due to the limited instrument payload on the NOAA Twin Otter. Average attenuation of  $\text{jNO}_2$  within  
260 the WF1 and WF2 plumes was 96% (meaning  $\text{jNO}_2$  at plume-center was 4 % of  $\text{jNO}_2$  outside of the plume). Plume-center



attenuation of  $j\text{NO}_2$  was 29% for the Castle plume. We sample the Cow plume after sunset and therefore do not have observation of  $j\text{NO}_2$  while the smoke was under sunlight (0 – 2 h). We estimate that plume-center  $j\text{NO}_2$  attenuation was 34%. This estimate was made by comparing  $j\text{NO}_2$  attenuation to plume size (by CO) in the WF and Castle model runs and is consistent with  $j\text{NO}_2$  attenuation in plumes emitted from the Cow fire sampled on other days. All other photolysis rates were estimated using a ratio of the observed  $j\text{NO}_2$  to calculated photolysis rates using an MCM trigonometric solar zenith angle (SZA) function below.

$$J = l * \cos(SZA)^m * e^{-n*\sec(SZA)} \quad (4)$$

Where  $l, m, n$  are derived from least squares fits to  $j$ -values from a radiative transfer model and literature cross sections/quantum yields. This calculation is a standard photolysis value method in FOAM and is described by Jenkin et al., 1997. However, this method does not account for overhead  $\text{O}_3$  column, surface albedo, aerosol or other effects. In all of the plumes studied here, observed  $j\text{NO}_2$  rates are below  $10^{-3} \text{ s}^{-1}$  excluding the first few minutes of the Castle plume (see Figure 2). Values of  $j\text{NO}_2$  in the WF2 plume remained low, near  $10^{-4} \text{ s}^{-1}$  during the sampling time. In contrast, the WF1 plume exhibits increasing  $j\text{NO}_2$  rates, which eventually reach  $8 \times 10^{-4} \text{ s}^{-1}$ . Differences in the photolysis rates between the first and second pass is likely due to the setting sun. Finally, observations of photolysis rates are negligible in the Cow plume as it was sampled after sunset.

### 2.3.3 Model Initiation

In all plumes except the Castle plume, our first transect sampled smoke 36 min – 2 h old and therefore we implemented an iterative method (McDuffie et al., 2018; Wagner et al., 2013) to estimate initial emissions (at age = 0). We began with best-guess estimates of CO, NO,  $\text{NO}_2$ , HONO and  $\text{O}_3$  then systematically changed these initial conditions to minimize the differences between model output and observations downwind. Initial conditions for all cases are shown in SI Table 4. In all cases, backgrounds of NO,  $\text{NO}_2$ ,  $\text{O}_3$ , CO and HONO were taken as an average outside of the plume and BBVOC backgrounds were assumed to be zero. Background mixing ratios used in all cases are shown in SI Table 2.

We determined best-guess estimates of CO and HONO directly from observations of the first transect. To determine a best-guess estimate for  $\text{NO}_x$  we used the sum of observed NO and  $\text{NO}_2$  for the Cow run or  $\text{NO}_y$  minus HONO (as  $\text{NO}_y$  will contain HONO) for the WF runs. Best-guess estimates of  $\text{O}_3$  were determined using an average of background  $\text{O}_3$  observations from a flight leg upwind of the fire and outside of the plume transects, which can vary (SI Table 5).

We began iteration with CO and  $k_{\text{dil}}$  by increasing best-guess estimates of CO and varying  $k_{\text{dil}}$  within the fit errors until we minimized the differences between observed and modeled CO. This in-turn determines the emissions of BBVOCs by Eq. (1). Next, we iterated  $\text{NO}_x$ , HONO and the NO/ $\text{NO}_x$  ratio such that the sum of  $\text{NO}_x$  and HONO did not exceed the observed  $\text{NO}_y$  and the initial NO/ $\text{NO}_x$  ratio remained between 0.6 – 1 (Roberts et al., 2020). Lastly, we iterated the initial and background  $\text{O}_3$ . As explained in section 2.4, we were required to iterate on background  $\text{O}_3$  in some model runs in order to achieve agreement



between model and observations. We repeated the above process to minimize the differences between model and observations. In an attempt to avoid finding a local solution, as opposed to the “best” solution, we reversed the order of iterating O<sub>3</sub>, NO<sub>x</sub> and HONO when repeating the above process.

Initial condition in the Castle run were taken directly from observations of NO, NO<sub>2</sub>, O<sub>3</sub>, CO, HONO, phenol, catechol, cresol, and methylcatechol in the first transect where the plume age was  $3 \pm 1$  min, and therefore was close to age = 0. We initiated the remaining 298 BBVOCs by using CO and Eq. (1).

## 2.4 Observations and Model Comparison

Accurately modeling the first order loss of CO is critical as it determines the overall plume dilution rate coefficient and initial BBVOC mixing ratios. Median differences in modeled and observed CO range from 39.7 – 307.4 ppbv with a median difference of 2.8 – 11.7 % across all model runs. Percentage and absolute differences between the model runs and observations are detailed in SI Table 6 and Figure 2. Median differences of NO<sub>2</sub> and HONO are 5.1 – 32.2 % and 6.6 – 53.3 %, respectively. There are greater percentage differences in NO<sub>2</sub> and HONO that arise due to lower mixing ratio observations mostly in the WF1 and Castle plumes, with a range of absolute median differences of NO<sub>2</sub> and HONO between 0.4 – 2.0 ppbv and 0.3 – 3.4 ppbv, respectively.

Ozone median differences vary from 0.3 – 6.3 ppbv with a median difference of 0.8 – 27.2 % across all runs. For the WF1 and WF2 plumes we found that a significant increase ( $38.5 \pm 0.4$  and  $35.3 \pm 7.5$  ppbv, SI Table 2 and SI Table 5) in model background O<sub>3</sub> compared to the upwind leg was required to capture the observed plume-center O<sub>3</sub>. This is due to photochemical O<sub>3</sub> production at the plume edges, where O<sub>3</sub> was as much as a factor of ~2 greater than the background O<sub>3</sub>. The increased plume edge O<sub>3</sub> is not captured in our plume-center model, and thus requires an increase in model background O<sub>3</sub>.

### 2.4.1. Comparisons of Constrained Compounds

The WF fire emissions were significantly greater than the Castle and Cow fire emissions as is seen in the observed CO (Figure 2). Initial plume-center CO was 8.26 and 8.33 ppmv in WF1 and WF2, respectively, but 2.62 and 1.95 ppmv for Cow and Castle, respectively.

We report our observations for each species (X) relative to CO in the form of normalized excess missing ratios (NEMR) following Yokelson et al., 2013 and shown in SI Figure 4.

$$\text{NEMR} = \frac{X_{\text{Plume}} - X_{\text{Background}} \text{ (ppbv)}}{\text{CO}_{\text{Plume}} - \text{CO}_{\text{Background}} \text{ (ppmv)}} \quad (5)$$

Ozone depression and negative NEMRs at the plume-center were observed in all of the sunset, nighttime or darkened fire plumes analyzed here. Observations of  $\Delta\text{O}_3/\Delta\text{CO}$  in the Castle plume remains at just below background levels of O<sub>3</sub> in all observations likely due to the small plume size and large O<sub>3</sub> background ( $82.5 \pm 2.1$  ppbv). Generally,  $\Delta\text{O}_3/\Delta\text{CO}$  increases



with plume age due to photochemical O<sub>3</sub> production and mixing with background O<sub>3</sub>. Ozone in the midday WF1 plume reaches 44.8 ± 3.4 ppbv ppmv<sup>-1</sup> of CO, or 67.4 ppbv above background, after 3.8 ± 0.5 h of transport.

Referring to SI Figure 4 we find that observed ΔNO/ΔCO, ΔNO<sub>2</sub>/ΔCO and ΔHONO/ΔCO have variable trends in all plumes. Observations of ΔNO/ΔCO are near zero (≤0.1 ppbv ppmv<sup>-1</sup>) in the Castle and WF1 plumes, and elevated in the WF2 and Cow plume (0.21 ± 0.02 – 1.21 ± 0.13 ppbv ppmv<sup>-1</sup>). Observed ΔNO/ΔCO in the WF2 plume change sharply between the first four and last five transects suggesting changes in fire emissions or photolysis near emission. In order to avoid these changes, we use only observations from the latter to constrain our model.

There is a general decrease of ΔNO<sub>2</sub>/ΔCO and ΔHONO/ΔCO over four hours of aging. Observations of ΔNO<sub>2</sub>/ΔCO in the WF1 plume decrease at a faster rate than those in the WF2 plume, however, both plumes exhibit about 8.6 ppbv ppmv<sup>-1</sup> in the youngest smoke (35 ± 8 min old).

#### 2.4.2. Comparisons of P(NO<sub>3</sub>)

Emissions of NO<sub>x</sub> from biomass burning plumes provide a source of NO<sub>3</sub> suggested to be a major oxidant for BBVOCs (Kodros et al., 2020). The instantaneous NO<sub>3</sub> production rate, P(NO<sub>3</sub>), is a common metric of the potential for NO<sub>3</sub> chemistry (Brown and Stutz, 2012).

$$P(\text{NO}_3) = k_{\text{NO}_3} [\text{NO}_2][\text{O}_3] \quad (6)$$

At the center of the plumes presented in this study, NO<sub>3</sub> production rates were between 0.1 and 1.5 ppbv h<sup>-1</sup> as seen in Figure 2. These NO<sub>3</sub> production rates are consistent with those found in a nighttime agricultural smoke plume measured above a rural area at the border of Missouri and Tennessee during the South East Nexus campaign (SENEX), which varied between 0.2 and 1.2 ppbv h<sup>-1</sup> (Decker et al., 2019). These values of P(NO<sub>3</sub>) are also similar to those found in urban plumes and forested areas. Production rates of NO<sub>3</sub> in urban plumes typically range within 0 – 3 ppbv h<sup>-1</sup> at night but can be larger. In forested regions, P(NO<sub>3</sub>) is typically below 1 ppbv h<sup>-1</sup> at night (Brown and Stutz, 2012).

Agreement between the model P(NO<sub>3</sub>) and observed P(NO<sub>3</sub>) reflects agreement between observed and modeled NO<sub>2</sub> and O<sub>3</sub>. The WF1 model run slightly overpredicts NO<sub>2</sub> after 3 hours of aging and therefore overpredicts P(NO<sub>3</sub>). Similarly, the Cow model run slightly underpredicts NO<sub>2</sub> compared to observations and therefore the trend in P(NO<sub>3</sub>) is slightly underpredicted.

#### 2.4.3 Comparison of phenolics

Our work focuses on the role of phenolics in BB plumes and includes updated and expanded phenolic oxidation mechanisms as described in the “Expansion of Phenolic Mechanism Description” in the SI. Therefore, capturing the phenolic evolution in our models is critical to understanding the importance of phenolics in BB. In the Castle case, which is initiated with observations of phenolics, we find excellent agreement for catechol, methycatechol, phenol, and cresol (SI Figure 5 and SI Figure 9). Further, we find that the model run lies on the upper edges of nitrocatechol errors, and the lower edge of nitrophenol errors. The model run underpredicts nitrocresol by a factor of 60. Note that we do not have available calibrations for



nitromethylcatechol, but do provide observations in arbitrary units for the purpose of comparing the time evolution of this compound.

355 Overall the model recreates the relative time evolution of nitrophenolics well. Disagreement between the model and observed compounds could be caused by many factors including, but not limited to, interfering isomers measured by the UW I<sup>-</sup> HR ToF CIMS or the NOAA I<sup>-</sup> ToF CIMS, variable fire ERs, and loss or production of nitrophenolics not captured by our mechanism. The MCM includes several gas-phase loss processes of nitrophenolics, but no gas to particle partitioning. Nitrophenolics readily partition to the aerosol phase (Finewax et al., 2018). Further, the MCM does not include photolytic loss of  
360 nitrophenolics, despite some evidence to the contrary (Sangwan and Zhu, 2016, 2018). Therefore, when analyzing gas phase nitrophenolic evolution we only consider integrated formation, as discussed in section 3.3.2.

All other model runs were not initiated to observations of phenolics due to the older age of smoke during the first transect. Even so, in the Cow model run (SI Figure 6 and SI Figure 10) we find agreement with catechol and methylcatechol within observation errors. Modeled phenol is about a factor of 3 ( $\Delta 1.4 - 2.0$  ppbv) greater than the observations. Modeled cresol is  
365 about a factor of 10 greater than observations, while its oxidation product, nitrocresol, is 7 times less than the observations. Models are thus able to reproduce some, but not all, phenolic observations in the Cow plume.

Observations of phenolics in the WF plumes are limited to un-calibrated catechol and nitrocatechol observations from the NOAA I<sup>-</sup> ToF CIMS (SI Figure 7 – SI Figure 8). In the WF1 model run, catechol and nitrocatechol appear to deplete faster than the model would suggest. The time evolution of nitrocatechol in the WF2 plume agrees well with the model, and in the  
370 WF1 model run the model matches the rough timing of the observed maximum signal.

### 3 Results and Discussion

#### 3.1 Reactivity

Instantaneous reactivity, Eq. (7) referred to simply as reactivity here on, is used as a simplified metric to predict the competition of reactions between oxidant and BBVOC

$$375 \quad k_X = \sum_i k_{X+BBVOC_i} [BBVOC_i] \quad (7)$$

where,  $k_{X+BBVOC}$  is a bimolecular rate coefficient for the reaction of X + BBVOC (where x is O<sub>3</sub>, NO<sub>3</sub> or OH) and  $k_X$  is an instantaneous first order rate coefficient. Here, we calculate and detail the reactivity for O<sub>3</sub>, NO<sub>3</sub> and OH oxidation of BBVOCs to understand their predicted competition. We also discuss how reactivity of the BB plumes studied here compare to other environments.

380 At emission, BBVOCs account for the majority of total reactivity for OH (87.7 %), NO<sub>3</sub> (80.1 %), and O<sub>3</sub> (99.6 %) as seen by the bars in Figure 3. HCHO and CO account for 5.1 % and 5.3 % of OH reactivity, respectively while NO<sub>2</sub> accounts for a small (0.3 %) fraction. We exclude O<sub>3</sub> reactivity to NO in Figure 3 because during the daytime this reaction is in a rapid cycle with



NO<sub>2</sub> photolysis and regeneration of O<sub>3</sub> in which odd oxygen, O<sub>x</sub> = NO<sub>2</sub> + O<sub>3</sub>, is conserved. Further reactions of O<sub>3</sub> and NO<sub>2</sub> can lead to loss of O<sub>x</sub>. This analysis includes BBVOC oxidation by O<sub>3</sub> but not a detailed budget for O<sub>x</sub>.

385 Underneath each reactivity bar in Figure 3 we show the partitioning of the initial BBVOC reactivity. Almost three quarters of OH reactivity is from alkenes (33.0 %), furans (25.0 %) and phenolics (16.4 %). The reactivity of NO<sub>3</sub>, by contrast, is controlled by phenolics (64.4 %) and O<sub>3</sub> reactivity is controlled by alkenes (53.8 %) and terpenes (39.2 %). Nitrate radical reactivity toward a smaller fraction of VOCs is consistent with other reactivity analyses of OH, NO<sub>3</sub> and O<sub>3</sub> in forest air (Palm et al., 2017).

390 Below each pie chart in Figure 3 we show reactivity for OH, NO<sub>3</sub>, and O<sub>3</sub> toward BBVOCs on an absolute scale. As BBVOCs are oxidized and the plume dilutes the plume reactivity is reduced. Decay of OH and NO<sub>3</sub> reactivity is nearly identical, while that of O<sub>3</sub> is different (e.g., WF2 and Dark). As a result, fewer BBVOCs, specifically alkenes, are oxidized in the Dark model run keeping reactivity greater when compared to the WF2 model run.

Total initial OH reactivity toward BBVOCs ranges from 98.3 – 450.0 s<sup>-1</sup>. Since the modeled total reactivity is proportional to  
395 the plume's initial emission of CO, the largest plumes, WF and Dark, have the greatest total initial total reactivity. Typical OH reactivities range between 7 – 130 s<sup>-1</sup> for urban plumes or 1 – 70 s<sup>-1</sup> in forests (Yang et al., 2016), demonstrating that wildfire plumes can be similar to urban plumes or significantly more reactive.

Total initial O<sub>3</sub> reactivity toward BBVOCs ranges between 1×10<sup>-4</sup> s<sup>-1</sup> and 6×10<sup>-4</sup> s<sup>-1</sup>. A recent study of a suburban site in China  
400 found O<sub>3</sub> reactivities toward non-methane VOCs between 2.5×10<sup>-7</sup> – 1.1×10<sup>-6</sup> s<sup>-1</sup> (Yang et al., 2020). Reactivity in wildfire plumes exceeds that in urban plumes by a factor of 80 – 3000.

Total initial NO<sub>3</sub> reactivity toward BBVOCs ranges from 17.1 – 70.3 s<sup>-1</sup>. Reactivity of NO<sub>3</sub> is typically reported as a lifetime (τ<sub>NO<sub>3</sub></sub>), which is the NO<sub>3</sub> concentration over the NO<sub>3</sub> production rate under the assumption of a steady state in both NO<sub>3</sub> and N<sub>2</sub>O<sub>5</sub> (Brown et al., 2003). Since NO<sub>3</sub> and N<sub>2</sub>O<sub>5</sub> readily interconvert (R4), the sum of τ<sub>NO<sub>3</sub></sub> and τ<sub>N<sub>2</sub>O<sub>5</sub></sub> are reported.

405 
$$\tau_{NO_3+N_2O_5} = \frac{NO_3+N_2O_5}{P(NO_3)} \quad (8)$$

Using Eq. (8), modeled steady-state lifetimes are predicted to be between 0.5 – 1.2 s. Typical τ<sub>NO<sub>3</sub></sub> in urban plumes range from  
tens of seconds to tens of minutes and τ<sub>NO<sub>3</sub></sub> in forested regions have been reported between 20 s – 15 min (Brown and Stutz,  
2012). The reactivity of NO<sub>3</sub> in wildfire plumes sampled during FIREX-AQ is 10 – 10<sup>4</sup> times greater than typical values in  
forested or urban environments. The increased reactivity of NO<sub>3</sub> to BBVOCs within wildfire plumes is greater than the  
410 increased reactivity for OH and O<sub>3</sub>, highlighting that BB plumes have large overall reactivity that is more pronounced for NO<sub>3</sub>  
than other oxidants.



In addition to a large suite of reactive BBVOCs that increase  $\text{NO}_3$  reactivity, smoke contains concentrations of aerosol and aerosol surface area that are far greater than normally found in urban areas (Decker et al., 2019). When considering  $\text{NO}_3$  reactivity we must also consider aerosols, since aerosols present a loss pathway for  $\text{NO}_3$  and its equilibrium product  $\text{N}_2\text{O}_5$  (Brown and Stutz, 2012; Goldberger et al., 2019). As explained in section 2.3.1 we calculate the  $\text{NO}_3$  heterogeneous reactivity to understand the competition between  $\text{NO}_3$  loss to BBVOCs and  $\text{NO}_3/\text{N}_2\text{O}_5$  heterogeneous loss to reaction with aerosol.

As shown in SI Figure 11 heterogeneous losses of  $\text{NO}_3$  and  $\text{N}_2\text{O}_5$  are  $<2\%$  of total  $\text{NO}_3$  reactivity in all model runs. Further, we find that  $>90\%$  of aerosol loss is through  $\text{N}_2\text{O}_5$  rather than  $\text{NO}_3$  uptake. Therefore heterogeneous losses of  $\text{NO}_3$  and  $\text{N}_2\text{O}_5$  do not appreciably compete with gas phase BBVOC oxidation, consistent with a similar analysis of nighttime smoke plumes (Decker et al., 2019).

While our analysis finds that the reactivity in a BB plume is far greater than other environments, it is important to note that our calculations use a large suite of the most reactive VOCs that may not be included in other reactivity studies. Further, our reactivity calculations are based on our BBVOC ER and kinetic database as described by Decker et al., 2019. While this database includes rate coefficients for the most reactive BBVOCs, it does not include rate coefficients for all 302 BBVOCs with all oxidants. Therefore, our reactivity estimates may be a lower estimate. Our VOC profile does not include alkanes, since FIREX lab studies (Hatch et al., 2015; Koss et al., 2018) and an OH reactivity analysis of FIREX lab emissions found that OH reactivity toward alkanes accounted for  $0 - 1\%$  of total BBVOC reactivity across all fuels (Gilman et al., 2015). Therefore, we expect the absent alkane reactivity in this study to be negligible.

### 3.2 Oxidation Rates

While reactivity is a useful metric to predict the competition between reactions, it does not account for oxidant concentration, which can vary widely depending on photolysis rates, emissions, and competing oxidants. In the following sections we discuss the BBVOC oxidation rate, which is related to reactivity through the oxidant concentration as shown below

$$R_x = \sum k_{X+\text{BBVOC}_i} [\text{BBVOC}_i][X] = k_x[X] \quad (9)$$

where  $R_x$  is the BBVOC oxidation rate,  $k_x$  is the biomolecular rate coefficient between X and BBVOC, and X is OH,  $\text{NO}_3$  or  $\text{O}_3$ . In the following sections we compare and contrast reactivity and oxidation budgets and discuss how the initial reactivity changes with plume age for different BBVOC groups. Finally, we discuss the oxidant competition between  $\text{NO}_3$ , OH, and  $\text{O}_3$  for three main groups of BBVOCs: phenolics, furans/furfurals, and alkenes/terpenes.

#### 3.2.1 Oxidation of BBVOCs

The integrated oxidation rate, or the oxidation budget (Figure 4), is similar to initial reactivity shown in Figure 3 for OH oxidation suggesting initial reactivity may be a good indicator for integrated reactivity. However, this does not hold true for  $\text{NO}_3$  or  $\text{O}_3$ .



The initial  $\text{NO}_3$  reactivity differs substantially from the oxidation budget. For example, 20 % of initial  $\text{NO}_3$  reactivity is due to  $\text{NO}$ , but  $\text{NO}$  accounts for  $\leq 1$  % of integrated  $\text{NO}_3$  loss. Further, photolysis of  $\text{NO}_3$  accounts for  $< 1$  % of  $\text{NO}_3$  loss in all model runs and is greatest in the Castle plume (0.6 %) where measured  $j\text{NO}_2$  and calculated  $j\text{NO}_3$  reached maximum values of  $4 \times 10^{-3}$  and  $0.14 \text{ s}^{-1}$ , respectively. Although daytime  $\text{NO}_3$  oxidation of reactive VOCs has been found for heavily polluted urban air (Brown et al., 2005; Geyer et al., 2003; Osthoff et al., 2006), the dominant  $\text{NO}_3$  loss processes in urban plumes is  $\text{NO}$  reaction and photolysis (Brown and Stutz, 2012; Wayne et al., 1991). The different controlling  $\text{NO}_3$  loss pathway here highlights the unique and highly reactive environment of BB plumes. Further, 67 – 70 % of integrated  $\text{NO}_3$  reaction is due to phenolics, which is larger than initial total  $\text{NO}_3$  reactivity (56 %). Integrated alkene, terpene, and furan oxidation by  $\text{NO}_3$  are all lower than their initial reactivities.

The production of  $\text{NO}_3$ , by (R3), and subsequent loss to BBVOCs is a significant (8 – 21 %) loss of  $\text{O}_3$ , and much greater than the initial  $\text{O}_3$  reactivity to  $\text{NO}_2$  of 0.4 %. Similarly, integrated loss of  $\text{O}_3$  to alkenes (40 – 49 %) and terpenes (16 – 23 %) is much less than initial reactivity would suggest (54 % and 39 %, respectively). Conversely, phenolics and furans account for 4 – 11 % and 13 – 20 % of  $\text{O}_3$  loss, respectively, even though their relative initial reactivity is  $< 1$  % and 7 %, respectively. Overall, the differences between initial reactivity and integrated oxidation rate are explained by changing reactivity as BBVOC are oxidized with plume age.

An example is seen in Figure 5 for  $\text{O}_3$  in the Castle model run, which has a large  $\text{O}_3$  background ( $72 \pm 1$  –  $82 \pm 2$  ppbv), is a relatively small plume, and is sunlit at emission. As a result, alkenes and terpenes are depleted quickly through oxidation by  $\text{O}_3$  and  $\text{OH}$ . The combined  $\text{O}_3$  reactivity of alkenes and terpenes reduces from 82 % to 44 % after two hours, during which time phenolic reactivity increases from  $< 1$  % to  $\sim 40$  %. In other words, as BBVOCs are depleted the reactivity profile of each oxidant will change and can result in significant differences between the initial reactivity and oxidant budget.

In contrast to  $\text{NO}_3$  and  $\text{O}_3$ , loss of  $\text{OH}$  by each BBVOC group is within 1 % of that predicted by the initial reactivity, except for terpenes. Initial reactivity of terpenes is about 13 %, while actual destruction of  $\text{OH}$  by terpenes averaged to 8 %. While terpene oxidation by  $\text{OH}$  is lower than its reactivity in all model runs, it is especially low (2 %) in the WF1 model run, which is likely due to the large concentration of  $\text{O}_3$  from photochemical production.

Losses of  $\text{OH}$  are not only due to highly reactive BBVOCs.  $\text{HCHO}$ ,  $\text{CO}$ , and  $\text{NO}_2$  are responsible for 12 – 14 % of  $\text{OH}$  destruction. This is consistent with an  $\text{OH}$  reactivity analysis from North American fuels burned during the FIREX laboratory study, which found  $13 \pm 1$  % of  $\text{OH}$  reactivity was due to  $\text{HCHO}$ ,  $\text{CO}$ , and  $\text{NO}_2$  (Gilman et al., 2015). The fraction of  $\text{OH}$  reactivity toward  $\text{CO}$  and  $\text{NO}_2$  are similar to those found in a tropical rainforest (Fuchs et al., 2017), but much smaller than the fraction of  $\text{OH}$  reactivity toward  $\text{CO}$  (7 %) and  $\text{NO}_2$  (18 %) found at an urban site (Gilman et al., 2009) and the fraction of  $\text{OH}$  reactivity toward  $\text{CO}$  (20 – 25 %) and  $\text{NO}_x$  (12 – 22 %) at a rural site (Edwards et al., 2013).

### 3.2.2 Oxidant Competition

To study the competition between all oxidants, we focus on three main BBVOC groups: phenolics, furans/furfurals, and alkenes/terpenes. Generally, furans/furfurals and alkenes/terpenes groups are mainly oxidized by  $\text{OH}$  and  $\text{O}_3$ , while  $\text{NO}_3$  plays



475 a small role (Figure 6). Oxidation of furans/furfurals and alkenes/terpenes by OH (18 – 55 %, 11 – 43 %, respectively) and O<sub>3</sub>  
(39 – 76 %, 54 – 88 %, respectively) can vary widely depending on the plume. We find this is due to the variability of actinic  
flux. In model runs with less photolysis at emission, OH oxidation is low compared to model runs that are more optically thin.  
This reduction of oxidation by OH appears to be replaced by O<sub>3</sub> rather than NO<sub>3</sub>. For example, relative furan/furfural oxidation  
by OH in the WF1 model run (relatively large integrated jNO<sub>2</sub>) is 31 % less than that in the Cow model run (comparatively  
480 lower integrated jNO<sub>2</sub>), yet O<sub>3</sub> oxidation is 32 % greater.

This relationship does not hold for phenolics, which are subject to significant NO<sub>3</sub> oxidation (26 – 52 %) (Figure 6). Phenolic  
oxidation by OH (22 – 43 %) and O<sub>3</sub> (16 – 33 %) are slightly less than NO<sub>3</sub>. As a result, phenolic oxidation by NO<sub>3</sub> dominates  
in the WF1 and Dark model runs, while OH dominates in the Castle model run. In the WF2 and Cow model runs, NO<sub>3</sub> and  
OH oxidation is roughly equal.

485 Generally, NO<sub>3</sub> oxidation of phenolics increases with O<sub>3</sub> availability and decreases with available actinic flux, but these  
relationships are coupled and complex. One example is seen in the WF2 model run, which has the second lowest integrated  
jNO<sub>2</sub> value, and large emissions of NO that keep O<sub>3</sub> low during sunlit hours. Therefore, P(NO<sub>3</sub>) is reduced, NO<sub>3</sub> is present at  
lower mixing ratios within the first hour of oxidation, and phenolics are less subject to NO<sub>3</sub> oxidation when compared to the  
other model runs.

490 As actinic flux increases so does OH and O<sub>3</sub> production, and therefore oxidant competition. One example is shown by the  
Castle model run where OH leads phenolic oxidation (41 %) with O<sub>3</sub> second (33 %). The Castle model run demonstrates the  
greatest observed background O<sub>3</sub> (90 ppbv). Further, the Castle model run has significantly smaller total emissions (based on  
CO) than the other model runs and the greatest integrated jNO<sub>2</sub>. Due to the increased background O<sub>3</sub> and photochemical  
production of OH, NO<sub>3</sub> plays a smaller role in the oxidation of phenolics.

### 495 **3.3 Phenolic Oxidation and Nitrophenolic Production**

The importance of phenolic oxidation for BB is evidenced by the rapidly growing literature (Bertrand et al., 2018; Chen et al.,  
2019; Coggon et al., 2019; Decker et al., 2019; Finewax et al., 2018; Gaston et al., 2016; Hartikainen et al., 2018; Iinuma et  
al., 2010; Lauraguais et al., 2014; Lin et al., 2015; Liu et al., 2019; Meng et al., 2020; Mohr et al., 2013; Palm et al., 2020;  
Selimovic et al., 2020; Wang and Li, 2021; Xie et al., 2017). Both OH and NO<sub>3</sub> oxidation of phenolics leads to nitrophenolics,  
500 which have been shown to significantly contribute to SOA production (Palm et al., 2020). However, not all nitrophenolics are  
created equal. Understanding the competition between phenolic oxidation by NO<sub>3</sub> and OH is critical because their oxidation  
pathways have significantly different implications for nitrogen budgets and total nitrophenolic yield. Nitrophenolics formed  
by OH requires one NO<sub>2</sub> molecule with a nitrophenolic yield between 27 – 33 %. In contrast nitrophenolics formed by NO<sub>3</sub>  
require two molecules of NO<sub>2</sub>, have a yield of 85 – 97 % and produce HNO<sub>3</sub> as a byproduct (see SI Figure 12 and Finewax et  
505 al., 2018).

Yet, current phenolic mechanisms are extremely limited. For example, in the MCM nitrophenolics are the only oxidation  
products of phenolics + NO<sub>3</sub> or OH and the yields are assumed to be 100%. Phenolic oxidation studies are typically limited to



510 final products without detailed examination of intermediates. Phenol and cresol reactions are well studied in comparison to catechol, methylcatechol, and higher order phenolics. For that reason, we use studies of phenol and cresol oxidation to extrapolate analogous branching ratios, rate coefficients, and products for catechol, methylcatechol, and three isomers of dimethylcatechol. All of these compounds are included in the MCM, but for the purpose of the following analysis we have expanded the phenolic reaction pathways in our model as explained in the SI and shown in SI Figure 12.

In the remaining sections, we detail how the competition for phenolic oxidation changes as the plume evolves over time. We then discuss the factors that cause differences in nitrophenolic production rate as well as how differences in OH and NO<sub>3</sub> phenolic oxidation lead to substantial differences in nitrocatechol yield. Finally, in the following section, we explore how nitrophenolics significantly impact the nitrogen budget.

### 3.3.1 Evolution of Phenolic Oxidation

520 Generally, the modeled total phenolic oxidation rate varies between 1-10 ppbv hr<sup>-1</sup> at emission (Figure 7 A – D), but the change in oxidation rate is not constant and trends with available actinic flux. Model runs with active initial photochemistry (Castle, WF2, and Cow) exhibit decreasing total oxidation rates, while model runs with little to no photolysis (WF1 and Dark) reach a local maximum rate after ~2 h and ~5 h, respectively. These increases in oxidation rate are due to increases in O<sub>3</sub> and NO<sub>3</sub> oxidation once NO is depleted.

525 Before sunset and in early stages of plume oxidation, the major channel of phenolic oxidation is via OH. However, in the WF1 model run NO<sub>3</sub> oxidation dominates after only 12 minutes (Figure 7 A). As the WF1 model run dilutes, photolysis rates increase and O<sub>3</sub> is entrained promoting O<sub>3</sub> and NO<sub>3</sub> production. This increase in oxidant concentration keeps phenolic oxidation > 1 ppbv h<sup>-1</sup> for at least four hours before the end of the model (see section 2.3), unlike other model runs that drop below 1 ppbv h<sup>-1</sup> of total phenolic oxidation within 0.5 - 3 h. After 2.6 h, in the WF1 model run, all oxidants contribute equally to phenolic oxidation and thereafter, OH and O<sub>3</sub> equally split oxidation while the influence of NO<sub>3</sub> decreases. At the end of the WF1 model run, 69% of initial phenolics remain unoxidized (SI Figure 13).

530 As the sun sets in our sunset model runs (WF2, Castle, and Cow) a transition from OH controlled to a mixture of NO<sub>3</sub> and O<sub>3</sub> controlled oxidation occurs when OH production, and total oxidation rate decrease rapidly. Interestingly, OH dominates phenolic oxidation in the Dark model run (initiated after sunset) for the first 1.8 h before NO<sub>3</sub> oxidation takes over. During this time, OH is produced by decomposition of Criegee intermediates formed through ozonolysis of unsaturated hydrocarbons, primarily catechol (SI Figure 12), methylcatechol and limonene. In other sunset model runs, OH plays a smaller role after sunset. Even so, this suggests that all BBVOC oxidation after sunset is driven by O<sub>3</sub> chemistry, either through direct oxidation by O<sub>3</sub>, NO<sub>2</sub> + O<sub>3</sub> to form NO<sub>3</sub>, or by formation and decomposition of Criegee intermediates to form OH.

540 The WF2, Dark, and Cow model runs all contain unreacted phenolic emissions at sunrise the following day (48%, 61%, and 8%, respectively, SI Figure 13). The WF2 and Dark model runs have significantly more phenolics that remain at sunrise because of their larger (~×3) emissions compared to the Cow model run. Further, the WF2 and Dark model run conditions differ only by the presence of photolysis and therefore the difference in remaining phenolics between the WF2 and Dark is



due to the time of day the smoke was emitted. In contrast to these three model runs, the emissions in Castle are depleted within 2.6 h due to its small size.

### 3.3.2 Total Nitrophenolic Formation

Nitrophenolic formation increases with  $O_3$  and photolysis, which promotes formation of  $NO_3$  and OH. For example, the Castle and Cow model runs have relatively large  $O_3$  and  $jNO_2$  at emission and therefore form nitrophenolics rapidly (0.6 – 1.4 ppbv  $h^{-1}$  within the first 15 min). In contrast, the WF and Dark model runs have near zero  $O_3$  due to large emissions of NO and relatively low or zero  $jNO_2$  and therefore form nitrophenolics more slowly ( $<0.1 - 0.7$  ppbv  $h^{-1}$  within the first 15 min).

Despite the rapid formation of nitrophenolics in the Castle model run, it has the least (excluding WF1) total nitrophenolic formation relative to total emissions as seen in Figure 8. Figure 8 shows integrated nitrophenolic formation per emitted ppmv of CO, which allows us to compare total nitrophenolic formation across varying plume sizes. In contrast to the Castle model run, the Cow model run has the greatest nitrophenolic formation. These differences are the result of differing phenolic oxidation pathways. The Castle model run has a large (90 ppbv)  $O_3$  background, which results in  $O_3$  accounting for ~40% of phenolic oxidation between 30 min – 2 h of age (Figure 7 C). At the end of the Castle model run (2.6 h)  $O_3$  oxidation accounts for 33% of total phenolic loss, the largest of any model run (Figure 6). This is markedly different than the Cow model run where OH and  $NO_3$  chemistry control phenolic oxidation before sunset, and  $NO_3$  after. While  $O_3$  accounts for only 16 % of phenolic loss at the end of the model run (~12 h). In our model, the reaction of  $O_3 +$  phenolics forms a ring opening product (SI Figure 12), but the rate coefficients and mechanisms are largely uncertain as discussed in the following section.

We include 157 phenolics in our above analysis, but only a few phenolics account for large fractions of nitrophenolic formation. At the end of our model runs, catechol and methylguaiacol account for the largest fraction of phenolic oxidation. Both compounds are mostly oxidized by  $NO_3$ . Catechol +  $NO_3$  alone accounts for 10 – 16 % of total phenolic oxidation rate or 30 – 32 % of  $NO_3 +$  phenolic oxidation. Similarly, methylguaiacol accounts for 22 – 26 % of  $NO_3 +$  phenolic rates and is the largest fraction of phenolic oxidation by OH (17 – 18 % of OH + phenolic rates). However, to our knowledge, oxidation products of methylguaiacol by OH and  $NO_3$  are unknown, but likely lead to nitrophenolics and therefore our nitrophenolic formation rates are likely underestimated.

### 3.3.3 Nitrocatechol Yield

The reaction of OH and  $NO_3$  with catechol to form nitrocatechol accounts for the largest fraction (32 – 33 %) of total nitrophenolic formation. Therefore, here, we focus on nitrocatechol and detail the nitrocatechol yield from  $NO_3$  and OH + catechol. Understanding nitrocatechol yield and its sensitivities is important to understanding the fate of  $NO_x$  and  $NO_x$  lifetime discussed in the final sections. However, the nitrocatechol yield depends on many variables such as the concentrations of  $NO_x$ , BBVOC,  $O_3$  and the  $NO_x$ /BBVOC ratio as well as the certainty in our chemical mechanisms. Therefore, we discuss the sensitivity of all of these factors on nitrocatechol yield below.



Yields of nitrocatechol vary between 33 – 45 % depending on the model run, where  $\text{NO}_3$  is responsible for the 72 – 92 % of nitrocatechol (Figure 9 A). Figure 9 explores factors that govern nitrocatechol yield, defined as the molar ratio of nitrocatechol production to catechol destruction. Yields of nitrocatechol from OH are low relative to  $\text{NO}_3$  yield due to the formation of trihydroxybenzene and benzoquinones (SI Figure 12), which account for 10 – 32 % and 4 – 5 % of total catechol loss, respectively.

The largest yield (45 %) is from the Dark model run, where  $\text{NO}_3$  oxidation accounts for more than 52 % of phenolic oxidation. In contrast, the lowest yield of nitrocatechol is from the Castle model run (33 %), which has the lowest emissions of  $\text{NO}_x$  compared to the other model runs. A similar yield (34 %) is found in the WF1 model run, however this model ends after only 4 h when 69 % of phenolics still remain. In short, nitrocatechol yield increases with increasing fraction of phenolic oxidation by  $\text{NO}_3$ .

To understand the dependence of nitrocatechol formation on  $\text{O}_3$ ,  $\text{NO}_x$ , total BBVOC emissions (defined by the sum of ERs in our BBVOC inventory) and BBVOC/ $\text{NO}_x$ , we ran a sensitivity analysis on the nitrocatechol yield (Figure 9 B – E). Based on emitted  $\text{NO}_x$  and CO, BBVOC/ $\text{NO}_x$  ratios in plumes we sample range from 11 – 35. However, due to fire variability, BBVOC emissions can vary by at least a factor of two and for many BBVOCs by more than a factor of 10 from our emission ratios (Decker et al., 2019). Furthermore, we only account for BBVOCs that are most reactive to  $\text{O}_3$ , OH, and  $\text{NO}_3$ , which is smaller than total emitted BBVOCs.

The nitrocatechol yield generally decreases with increasing BBVOC/ $\text{NO}_x$  (color scale and white lines in Figure 9 B). As expected, nitrocatechol yields increase with increasing  $\text{NO}_x$  (Figure 9 C). Across all model runs, the nitrocatechol yield increases to 43 % – 57 % over a  $\text{NO}_x$  range of 4.2 – 91.2 ppbv. Further, the nitrocatechol yield changes to 27 % – 50 % (Figure 9 D) when varying total BBVOC emissions by a factor 0.5 – 4. Finally, we investigate the sensitivity of nitrocatechol yield to initial  $\text{O}_3$  and find that all model runs have little sensitivity to  $\text{O}_3$  (Figure 9 E) with an absolute change in nitrocatechol yield <3 % for all model runs when varying initial  $\text{O}_3$  over a range of 0 – 113 ppbv.

The low sensitivity of nitrocatechol yield to  $\text{O}_3$  may be partially explained by competition between  $\text{O}_3$  and  $\text{NO}_3$  + phenolic reactions after sunset. To explore this, we use framework developed by Edwards et al., 2017. Briefly, as stated in section 3.3.1, BBVOCs are the main sink for  $\text{NO}_3$  and therefore  $\text{NO}_3$  loss rate is controlled by the  $\text{NO}_3$  formation rate. As a result,  $\text{NO}_3$  can be considered to be in approximate steady state between production by  $\text{NO}_2 + \text{O}_3$  and loss by  $\text{NO}_3 + \text{BBVOC}$ . Further, according to Figure 4, the majority of  $\text{NO}_3$  is lost to phenolics. As a result, the rate of phenolic oxidation after sunset (when OH oxidation of phenolics is minimized) can be approximated as

$$-\frac{d[\text{phenolics}]}{dt} \approx (k_{\text{O}_3} [\text{phenolics}] + k_{\text{NO}_2+\text{O}_3} [\text{NO}_2])[\text{O}_3] \quad (9)$$

which shows that the dominant oxidant is determined by the ratio of  $\text{NO}_2$  and phenolics. We find that the ratio of phenolics to  $\text{NO}_2$  at which  $\text{NO}_3$  and  $\text{O}_3$  oxidation is equal to be  $\sim 10$  (at 298 K, using an ER weighted average  $k_{\text{O}_3} = 2.6 \times 10^{-18} \text{ cm}^3 \text{ molecule}^{-1} \text{ s}^{-1}$ ) with  $\text{NO}_3$  oxidation more important below this ratio, and  $\text{O}_3$  oxidation more important above it. Modeled phenolics/ $\text{NO}_2$



ratios at sunset range between 0.7 – 1.2 and in all model runs, except the Castle model run, the ratio decreases with age. This  
605 suggests that in all model runs NO<sub>3</sub> oxidation is expected to control phenolic oxidation after sunset.

The phenolic oxidation analysis above relies on phenolic mechanisms and rate coefficients that are highly uncertain. For  
example, the above calculated ratio could be much lower in cold lofted plumes, but knowledge of temperature dependent O<sub>3</sub>  
+ phenolic rate coefficients are unavailable. Using temperatures observed in the WF2 plume (~268 K) for k<sub>NO<sub>2</sub>+O<sub>3</sub></sub> the  
phenolics to NO<sub>2</sub> ratio at which NO<sub>3</sub> and O<sub>3</sub> oxidation is equal would be ~ 4.

610 The rate coefficient and products for the reaction of catechol + O<sub>3</sub> that we use are generated using MCM mechanism  
methodology (Jenkin et al., 2003; Saunders et al., 2003). An experimental study on the gas-phase reaction of catechol + O<sub>3</sub>  
finds an RH dependent rate coefficient that decreases non-linearly from 1.3×10<sup>-17</sup> to 1.2×10<sup>-19</sup> cm<sup>3</sup> molecule<sup>-1</sup> s<sup>-1</sup> with  
increasing RH (El Zein et al., 2015). The MCM uses a rate coefficient of 9.2×10<sup>-18</sup> cm<sup>3</sup> molecule<sup>-1</sup> s<sup>-1</sup>. Further, to our  
knowledge there are no experimental kinetic or mechanistic studies of phenol + O<sub>3</sub>. In the plumes we investigate, RH varied  
615 between roughly 20 – 60 %. Using an RH dependent rate coefficient for O<sub>3</sub> + catechol we find that the nitrocatechol yields  
range between 31 – 58 % with little change in yield for the Castle model run (-2 %) and larger change for the Dark model run  
(+13 %).

### 3.4 Fate of NO<sub>x</sub> in Dark BB Plumes

Fire emissions are concentrated sources of NO<sub>x</sub>, but as a result of photochemistry and oxidation the loss processes and lifetime  
620 of plume NO<sub>x</sub> are variable. Photochemical NO<sub>x</sub> loss pathways include reaction with OH (R8), net formation of peroxy acyl  
nitrates (PANs) (R9), and formation of organic nitrates (R10).



625 The NO<sub>x</sub> rate consumption is further influenced by the formation and the subsequent fate of NO<sub>3</sub> (R1 – 3, 4, 6 – 7).  
Heterogeneous uptake of N<sub>2</sub>O<sub>5</sub> (R5) and production of nitrophenolics double the NO<sub>x</sub> consumption rate since in both cases  
subsequent chemistry consumes one additional NO<sub>2</sub> molecule, with the rate limiting step being (R3). Below, we focus on the  
products of NO<sub>x</sub> oxidation, determined as NO<sub>z</sub> = NO<sub>y</sub> – NO<sub>x</sub>.

Results are similar for all model runs, and we discuss the WF2 model run as a case study. While a complete NO<sub>z</sub> budget  
630 analysis constrained to observations is beyond the scope of this work, we compare our model results of PAN, (peroxy acetyl  
nitrate, a component of PANs) to observations (SI Figure 8). PAN accounts for ~65% of PANs, and PANs account for the  
largest fraction of NO<sub>z</sub> in our model runs during sunlit hours. Our model reproduces PAN well in one transect, but  
underpredicts PAN by a factor of ~2.5 in others. Similar to O<sub>3</sub> (section 2.3.2), PAN is enhanced on plume edges and the  
enhancement likely mixes into the center, which is not captured by our model runs. Therefore, we constrain our model to PAN



635 observations, present an average result (Figure 10), and consider our model unconstrained to PAN to be a lower-bound PAN estimate and our model constrained to PAN to be an upper-bound PAN estimate.

### 3.4.1 NO<sub>z</sub> Budgets

The late day emitted plumes modeled in this paper exhibit photochemical loss of NO<sub>x</sub> initially. In the period prior to sunset, PANs and PNA (peroxynitric acid, HO<sub>2</sub>NO<sub>2</sub>) dominate NO<sub>z</sub> and PANs alone accounts for 51 ± 6 % of NO<sub>z</sub> by sunset. The  
640 WF2 plume is lofted, and therefore cold (~267 K), which results in a long PAN and PNA lifetime (~150 h, and ~0.4 h respectively). Even so, as these plumes continue to age, PANs and PNA decompose slowly (Figure 10) to provide NO<sub>2</sub> that promotes nitrophenolic formation and increases nitrophenolic yield (see section 3.3.3). The increase in NO<sub>2</sub> after sunset promotes CH<sub>3</sub>O<sub>2</sub>NO<sub>2</sub> as well as NO<sub>3</sub> chemistry products, which grow steadily overnight. The contribution of PANs and PNA to NO<sub>z</sub> decreases from 71 ± 6 % at sunset to 17 ± 2 % at sunrise. Relative NO<sub>x</sub> loss to PANs and PNA is mostly replaced by  
645 the formation of nitrophenolics (Δ 19 ± 1 %), HNO<sub>3</sub> by NO<sub>3</sub> chemistry (Δ 22 %), and other or unknown NO<sub>3</sub> products (Δ 11 %) overnight.

After sunset NO<sub>3</sub> chemistry takes over and by sunrise NO<sub>3</sub> chemistry products lead the (66 ± 2 %) NO<sub>z</sub> budget. Nitrophenolic formation accounts for 56 ± 2 % of NO<sub>z</sub> in the form of HNO<sub>3</sub> and nitrophenolics where nitrophenolics alone account for 29 ± 1 % of NO<sub>z</sub>. Total HNO<sub>3</sub> formation accounts for 31 ± 1 % of NO<sub>z</sub>, however most (88 %) of HNO<sub>3</sub> results from NO<sub>3</sub>  
650 chemistry. Despite accounting for only 9% (by mole) of initial emissions in our model runs, phenolics have a large and disproportionate effect on NO<sub>x</sub> loss at night.

A similar example is seen in the Dark model run (SI Figure 16), where PANs and PNA dominate NO<sub>z</sub> budget for 2.3 h until NO is depleted. At this time, PNA and PANs steadily decrease while NO<sub>3</sub> products steadily increase throughout the night. By sunrise the next day, NO<sub>3</sub> chemistry products (including unknown products) account for 80 % of NO<sub>z</sub>. In all model runs there  
655 is a significant (12 – 16 %) NO<sub>z</sub> formed through NO<sub>3</sub> chemistry that leads to unknown products. These unknown products are primarily the result of NO<sub>3</sub> + heterocycles such as furans and pyrroles, which have published rate coefficients but little mechanistic work in the literature.

### 3.4.2 NO<sub>x</sub> Lifetime

The availability of O<sub>3</sub> and sunlight at emission strongly affects NO<sub>x</sub> lifetime ( $\tau_{NO_x}$ , Figure 11) defined below

$$660 \quad \tau_{NO_x} = \frac{1}{\sum_i k_i} \quad (11)$$

where  $k_i$  is a unimolecular rate coefficient for (R3, 8 – 10). Model runs with relatively large photolysis and O<sub>3</sub> at emission (Castle, Cow, and WF1) have near emission  $\tau_{NO_x}$  that range from 1 – 3 h (Figure 11), which are accompanied by larger total oxidation rates for all BBVOCs (SI Figure 13 – SI Figure 15). These model runs also exhibit the fastest nitrophenolic formation rates (section 3.3.2 and Figure 8). In contrast model runs with low or zero photolysis and near zero O<sub>3</sub> (WF2 and Dark) exhibit  
665 near emission  $\tau_{NO_x} = \sim 10 - 16$  h and  $\tau_{NO_x} = 20 - 150$  h, respectively. The absence of photolysis in the Dark model run explains



the large difference in  $\tau_{NO_x}$  between the WF2 and Dark model runs as the WF2 model run has greater  $O_3$  and  $P(NO_3)$  that promotes  $NO_3$  chemistry as well as OH radical that promotes PANs formation. Once NO is depleted in both model runs  $NO_x$  chemistry changes. The BBVOCs oxidation rate rapidly increases (SI Figure 13 – SI Figure 15) and  $NO_x$  loss switches from primarily PAN and PNA to nitrophenolic production as the sun sets (Figure 10) and  $O_3$  is entrained from the background. As such,  $\tau_{NO_x}$  decreases markedly to  $\sim 0.5$  h.

Due to their reduced oxidation rates at emission, the WF2 and Dark model runs retain about half (46% and 57 %, respectively) of the emitted  $NO_x$  by sunrise the next day. Here, we calculate remaining  $NO_x$  as the fraction of  $NO_x$  remaining at the end of our model divided by the amount of  $NO_x$  that was reacted, excluding dilution. This is about a  $\Delta NO_x / \Delta CO$  of  $\sim 4$  ppbv  $ppmv^{-1}$  at sunrise, which is similar to the initial emissions of Castle ( $\sim 6$  ppbv  $ppmv^{-1}$ ) and WF1 ( $\sim 5$  ppbv  $ppmv^{-1}$ ). Further, at sunrise, we expect the WF2 and Dark plumes to be more optically transparent and free of NO, and thus oxidation rates to increase rapidly as they both still contain  $NO_x$ . An increase in oxidation at sunrise will likely be more important for the Dark model run, as it retains 61% of the emitted phenolics as opposed to 48 % in the WF2 model run. Plumes emitted after sunset have slower oxidation rates compared to daytime plumes (section 3.2), but undergo additional oxidation from evening to morning. However, outside of the plume-center, where  $O_3$  is less effected by reaction with NO and is more likely to be generated by photochemical production,  $NO_x$  loss rates may be much larger. Therefore,  $NO_x$  away from the plume-center will likely be depleted more rapidly.

#### 4 Conclusions

This study details the competitive oxidation of BBVOCs in four near-sunset, or low-photolysis, smoke plumes sampled by the NOAA Twin Otter or the NASA DC-8 aircraft during the FIREX-AQ 2019 field campaign. We model these plumes, as well as a theoretical dark plume, using an observationally constrained 0-D chemical box model. Our model suggests OH is reactive to most BBVOCs, while  $NO_3$  is most reactive to phenolics, and  $O_3$  to alkenes and terpenes. We find that initial reactivity is a good indicator for subsequent oxidation by OH, but not for  $NO_3$  and  $O_3$ . For example, unlike urban plumes, we find that  $NO_3$  loss to NO, photolysis and heterogeneous uptake are negligible loss pathways, and that most ( $\geq 98$  %) of  $NO_3$  loss occurs through BBVOC oxidation.

Phenolics are the only BBVOC group for which oxidation by  $NO_3$ , OH, and  $O_3$  is competitive. Specifically,  $NO_3$  is responsible for 26 – 52 % of phenolic loss and leads (36%) phenolic oxidation in an optically thick mid-day plume. In addition, all phenolic oxidation after sunset is dependent on  $O_3$ , whether through direct oxidation by  $O_3$ , production of  $NO_3$  by  $NO_2 + O_3$ , or ozonolysis of unsaturated hydrocarbons and subsequent decomposition to OH radicals.

We find  $NO_3$  chemistry is responsible for 72 – 92 % (84 % in an optically thick mid-day plume) of nitrocatechol formation and controls nitrophenolic formation overall. Ultimately, nitrophenolic formation pathways account for 58 – 66 % of  $NO_x$  loss by sunrise the following day. Formation of nitrophenolics by  $NO_3$ , as opposed to OH, is the largest  $NO_x$  sink and accounts for most of the inorganic and organic nitrogen at the end of the night. While both PANs and PNA account for most of the  $NO_x$



700 loss shortly after emission, they decompose overnight providing a  $\text{NO}_x$  source for nitrophenolic formation and increase nitrocatechol yield. In short,  $\text{NO}_3$  chemistry should be considered, even during the daytime, when investigating BB plume oxidation as we find it is the main source of nitrophenolic formation in plumes studied here and thus may be a dominant pathway to SOA formation.

### Author Contributions

705 FIREX-AQ data were measured and processed by the following people: UW I- HR ToF CIMS (ZCJD, CDF, BBP, JAT); Tenax (KCB, PVR); Picarro G2401-m (MAR, SSB); NCAR CL (FMF, DDM, GST, AJW); UHSAS (AF, AMM);  $\text{jNO}_2$  on the Twin Otter (MAR); CO by diode laser (JPD, GSD, HH, JBW); CO by CES (JP); NOAA CL (IB, JP, TBR); ACES (SSB, MAR, JL, CW); NOAA LIF (PSR, AWR); NOAA I- ToF CIMS (JAN, PRV); PAN (LGH, YRL); SMPS/LAS (RHM, LT, El. Wi, Ed Wi); CAFS (SH, KU); smoke ages (CDH). Updates to the phenolic mechanism were performed by MMC, ZCJD, MAR, RHS. Model runs were conducted by ZCJD. Preparation of the manuscript was done by ZCJD with contributions from coauthors.

### 710 Competing Interests

The authors declare that they have no conflict of interest.

### Acknowledgements

715 Thank you to Alan Fried, Dirk Richter, Jim Walega, and Petter Weibring for use of their HCHO measurements. A big thank you to all of those who helped organize and participated in the 2019 FIREX-AQ field campaign, specifically the NOAA Aircraft Operations, including Francisco Fuenmayor, Joe Greene, Conor Maginn, Rob Miletic, Joshua Rannenberg, and David Reymore. Carley D. Fredrickson, Brett B. Palm, and Joel A. Thornton were supported by NOAA OAR Climate Program Office Award Number NA17OAR4310012.

### Financial Support

720 Carley D. Fredrickson, Brett B. Palm, and Joel A. Thornton were supported by NOAA OAR Climate Program Office Award Number NA17OAR4310012.



## References

- Abatzoglou, J. T. and Williams, A. P.: Impact of anthropogenic climate change on wildfire across western US forests, *Proc. Natl. Acad. Sci.*, 113(42), 11770–11775, doi:10.1073/pnas.1607171113, 2016.
- 725 Akagi, S. K., Yokelson, R. J., Wiedinmyer, C., Alvarado, M. J., Reid, J. S., Karl, T., Crounse, J. D. and Wennberg, P. O.: Emission factors for open and domestic biomass burning for use in atmospheric models, *Atmos. Chem. Phys.*, 11(9), 4039–4072, doi:10.5194/acp-11-4039-2011, 2011.
- Andreae, M. O. and Merlet, P.: Emissions of trace gases and aerosols from biomass burning, *Biogeochemistry*, 15(4), 955–966, 2001.
- 730 Balch, J. K., Bradley, B. A., Abatzoglou, J. T., Chelsea Nagy, R., Fusco, E. J. and Mahood, A. L.: Human-started wildfires expand the fire niche across the United States, *Proc. Natl. Acad. Sci. U. S. A.*, 114(11), 2946–2951, doi:10.1073/pnas.1617394114, 2017.
- Barbero, R., Abatzoglou, J. T., Larkin, A. N., Kolden, C. A. and B., S.: Climate change presents increased potential for very large fires in the contiguous United States, *Int. J. Wildl. Fire*, 24(7), 892–899, 2015.
- 735 Bertrand, A., Stefenelli, G., Jen, C. N., Pieber, S. M., Bruns, E. A., Ni, H., Temime-Roussel, B., Slowik, J. G., Goldstein, A. H., El Haddad, I., Baltensperger, U., Prévôt, A. S. H., Wortham, H. and Marchand, N.: Evolution of the chemical fingerprint of biomass burning organic aerosol during aging, *Atmos. Chem. Phys.*, 18(10), 7607–7624, doi:10.5194/acp-18-7607-2018, 2018.
- Bishop, G. A. and Haugen, M. J.: The Story of Ever Diminishing Vehicle Tailpipe Emissions as Observed in the Chicago, Illinois Area, *Environ. Sci. Technol.*, 52(13), 7587–7593, doi:10.1021/acs.est.8b00926, 2018.
- 740 Bloss, C., Wagner, V., Jenkin, M. E., Volkamer, R., Bloss, W. J., Lee, J. D., Heard, D. E., Wirtz, K., Martin-Reviejo, M., Rea, G., Wenger, J. C. and Pilling, M. J.: Development of a detailed chemical mechanism (MCMv3.1) for the atmospheric oxidation of aromatic hydrocarbons, *Atmos. Chem. Phys.*, 5(3), 641–664, doi:10.5194/acp-5-641-2005, 2005.
- Bolzacchini, E., Bruschi, M., Hjorth, J., Meinardi, S., Orlandi, M., Rindone, B. and Rosenbohm, E.: Gas-Phase Reaction of
- 745 Phenol with NO<sub>3</sub>, *Environ. Sci. Technol.*, 35, 1791–1797, 2001.
- Brey, S. J., Barnes, E. A., Pierce, J. R., Wiedinmyer, C. and Fischer, E. V.: Environmental Conditions, Ignition Type, and Air Quality Impacts of Wildfires in the Southeastern and Western United States, *Earth's Futur.*, 6(10), 1442–1456, doi:10.1029/2018EF000972, 2018.
- Brown, S. S. and Stutz, J.: Nighttime radical observations and chemistry, *Chem. Soc. Rev.*, 41, 6405–6447, doi:10.1039/c2cs35181a, 2012.
- 750 Brown, S. S., Stark, H. and Ravishankara, A. R.: Applicability of the steady state approximation to the interpretation of atmospheric observations of NO<sub>3</sub> and N<sub>2</sub>O<sub>5</sub>, *J. Geophys. Res.*, 108(D17), 4539, doi:10.1029/2003JD003407, 2003.
- Brown, S. S., Osthoff, H. D., Stark, H., Dubé, W. P., Ryerson, T. B., Warneke, C., de Gouw, J. A., Wollny, A. G., Parrish, D. D., Fehsenfeld, F. C. and Ravishankara, A. R.: Aircraft observations of daytime NO<sub>3</sub> and N<sub>2</sub>O<sub>5</sub> and their implications for



- 755 tropospheric chemistry, *J. Photochem. Photobiol. A Chem.*, 176(1-3 SPEC. ISS.), 270–278, doi:10.1016/j.jphotochem.2005.10.004, 2005.
- Calvert, J. G., Mellouki, A., Orlando, J. J., Pilling, M. J. and Wallington, T. J.: Mechanisms of Atmospheric Oxidation of the Oxygenate., 2011.
- Chang, W. L., Bhave, P. V., Brown, S. S., Riemer, N., Stutz, J. and Dabdub, D.: Heterogeneous atmospheric chemistry, ambient  
760 measurements, and model calculations of N<sub>2</sub>O<sub>5</sub>: A review, *Aerosol Sci. Technol.*, 45(6), 655–685, doi:10.1080/02786826.2010.551672, 2011.
- Chen, X., Sun, Y., Qi, Y., Liu, L., Xu, F. and Zhao, Y.: Mechanistic and kinetic investigations on the ozonolysis of biomass burning products: Guaiacol, syringol and creosol, *Int. J. Mol. Sci.*, 20(18), doi:10.3390/ijms20184492, 2019.
- Coggon, M. M., Lim, C. Y., Koss, A. R., Sekimoto, K., Yuan, B., Gilman, J. B., Hagan, D. H., Selimovic, V., Zarzana, K. J.,  
765 Brown, S. S., M Roberts, J., Müller, M., Yokelson, R., Wisthaler, A., Krechmer, J. E., Jimenez, J. L., Cappa, C., Kroll, J. H., De Gouw, J. and Warneke, C.: OH chemistry of non-methane organic gases (NMOGs) emitted from laboratory and ambient biomass burning smoke: Evaluating the influence of furans and oxygenated aromatics on ozone and secondary NMOG formation, *Atmos. Chem. Phys.*, 19(23), 14875–14899, doi:10.5194/acp-19-14875-2019, 2019.
- Crosson, E. R.: A cavity ring-down analyzer for measuring atmospheric levels of methane, carbon dioxide, and water vapor,  
770 *Appl. Phys. B Lasers Opt.*, 92(3 SPECIAL ISSUE), 403–408, doi:10.1007/s00340-008-3135-y, 2008.
- Decker, Z. C. J., Zarzana, K. J., Coggon, M., Min, K.-E., Pollack, I., Ryerson, T. B., Peischl, J., Edwards, P., Dubé, W. P., Markovic, M. Z., Roberts, J. M., Veres, P. R., Graus, M., Warneke, C., de Gouw, J., Hatch, L. E., Barsanti, K. C. and Brown, S. S.: Nighttime Chemical Transformation in Biomass Burning Plumes: A Box Model Analysis Initialized with Aircraft Observations, *Environ. Sci. Technol.*, 53(5), 2529–2538, doi:10.1021/acs.est.8b05359, 2019.
- 775 Dennison, P. E., Brewer, S. C., Arnold, J. D. and Moritz, M. A.: Large wildfire trends in the western United States, 1984–2011, *Geophys. Res. Lett.*, 41, 2014GL059576, doi:10.1002/2014gl059576, 2014.
- Edwards, P. M., Evans, M. J., Furneaux, K. L., Hopkins, J., Ingham, T., Jones, C., Lee, J. D., Lewis, A. C., Moller, S. J., Stone, D., Whalley, L. K. and Heard, D. E.: OH reactivity in a South East Asian tropical rainforest during the oxidant and particle photochemical processes (OP3) project, *Atmos. Chem. Phys.*, 13(18), 9497–9514, doi:10.5194/acp-13-9497-2013, 2013.
- 780 Eilerman, S. J., Peischl, J., Neuman, J. A., Ryerson, T. B., Aikin, K. C., Holloway, M. W., Zondlo, M. A., Golston, L. M., Pan, D., Floerchinger, C. and Herndon, S.: Characterization of Ammonia, Methane, and Nitrous Oxide Emissions from Concentrated Animal Feeding Operations in Northeastern Colorado, *Environ. Sci. Technol.*, 50(20), 10885–10893, doi:10.1021/acs.est.6b02851, 2016.
- Finewax, Z., De Gouw, J. A. and Ziemann, P. J.: Identification and Quantification of 4-Nitrocatechol Formed from OH and  
785 NO<sub>3</sub> Radical-Initiated Reactions of Catechol in Air in the Presence of NO<sub>x</sub>: Implications for Secondary Organic Aerosol Formation from Biomass Burning, *Environ. Sci. Technol.*, 52(4), 1981–1989, doi:10.1021/acs.est.7b05864, 2018.
- Fuchs, H., Tan, Z., Lu, K., Bohn, B., Broch, S., Brown, S. S., Dong, H., Gomm, S., Häsel, R., He, L., Hofzumahaus, A., Holland, F., Li, X., Liu, Y., Lu, S., Min, K. E., Rohrer, F., Shao, M., Wang, B., Wang, M., Wu, Y., Zeng, L., Zhang, Y.,



- 790 Wahner, A. and Zhang, Y.: OH reactivity at a rural site (Wangdu) in the North China Plain: Contributions from OH reactants and experimental OH budget, *Atmos. Chem. Phys.*, 17(1), 645–661, doi:10.5194/acp-17-645-2017, 2017.
- Gaston, C. J., Lopez-Hilfiker, F. D., Whybrew, L. E., Hadley, O., McNair, F., Gao, H., Jaffe, D. A. and Thornton, J. A.: Online molecular characterization of fine particulate matter in Port Angeles, WA: Evidence for a major impact from residential wood smoke, *Atmos. Environ.*, 138, 99–107, doi:10.1016/j.atmosenv.2016.05.013, 2016.
- 795 Geyer, A., Alicke, B., Ackermann, R., Martinez, M., Harder, H., Brune, W., Di Carlo, P., Williams, E., Jobson, T., Hall, S., Shetter, R. and Stutz, J.: Direct observations of daytime NO<sub>3</sub>: Implications for urban boundary layer chemistry, *J. Geophys. Res. Atmos.*, 108(12), 1–11, doi:10.1029/2002jd002967, 2003.
- Giglio, L.: Characterization of the tropical diurnal fire cycle using VIRS and MODIS observations, *Remote Sens. Environ.*, 108(4), 407–421, doi:10.1016/j.rse.2006.11.018, 2007.
- 800 Gilman, J. B., Kuster, W. C., Goldan, P. D., Herndon, S. C., Zahniser, M. S., Tucker, S. C., Brewer, W. A., Lerner, B. M., Williams, E. J., Harley, R. A., Fehsenfeld, F. C., Warneke, C. and De Gouw, J. A.: Measurements of volatile organic compounds during the 2006 TexAQS/GoMACCS campaign: Industrial influences, regional characteristics, and diurnal dependencies of the OH reactivity, *J. Geophys. Res. Atmos.*, 114(7), 1–17, doi:10.1029/2008JD011525, 2009.
- 805 Gilman, J. B., Lerner, B. M., Kuster, W. C., Goldan, P. D., Warneke, C., Veres, P. R., Roberts, J. M., De Gouw, J. A., Burling, I. R. and Yokelson, R. J.: Biomass burning emissions and potential air quality impacts of volatile organic compounds and other trace gases from fuels common in the US, *Atmos. Chem. Phys.*, 15(24), 13915–13938, doi:10.5194/acp-15-13915-2015, 2015.
- Goldberger, L. A., Jahl, L. G., Thornton, J. A. and Sullivan, R. C.: N<sub>2</sub>O<sub>5</sub> reactive uptake kinetics and chlorine activation on authentic biomass-burning aerosol, *Environ. Sci. Process. Impacts*, 21(10), 1684–1698, doi:10.1039/c9em00330d, 2019.
- 810 Hartikainen, A., Yli-Pirilä, P., Tiitta, P., Leskinen, A., Kortelainen, M., Orasche, J., Schnelle-Kreis, J., Lehtinen, K., Zimmermann, R., Jokiniemi, J. and Sippula, O.: Volatile organic compounds from logwood combustion: Emissions and transformation under dark and photochemical aging conditions in a smog chamber, *Environ. Sci. Technol.*, 52(4979–4988), acs.est.7b06269, doi:10.1021/acs.est.7b06269, 2018.
- Hatch, L. E., Luo, W., Pankow, J. F., Yokelson, R. J., Stockwell, C. E. and Barsanti, K. C.: Identification and quantification of gaseous organic compounds emitted from biomass burning using two-dimensional gas chromatography–time-of-flight mass spectrometry, *Atmos. Chem. Phys.*, 15(4), 1865–1899, doi:10.5194/acp-15-1865-2015, 2015.
- 815 Hatch, L. E., Yokelson, R. J., Stockwell, C. E., Veres, P. R., Simpson, I. J., Blake, D. R., Orlando, J. J. and Barsanti, K. C.: Multi-instrument comparison and compilation of non-methane organic gas emissions from biomass burning and implications for smoke-derived secondary organic aerosol precursors, *Atmos. Chem. Phys.*, 17(2), 1471–1489, doi:10.5194/acp-17-1471-2017, 2017.
- 820 Hatch, L. E., Rivas-ubach, A., Jen, C. N., Lipton, M., Goldstein, A. H. and Barsanti, K. C.: Measurements of I / SVOCs in biomass-burning smoke using solid-phase extraction disks and two-dimensional gas chromatography, *Atmos. Chem. Phys.*, 18, 17801–17817, doi:10.5194/acp-18-17801-2018, 2018.
- Higuera, P. E., Abatzoglou, J. T., Littell, J. S. and Morgan, P.: The changing strength and nature of fire-climate relationships



- in the northern Rocky Mountains, U.S.A., 1902–2008, *PLoS One*, 10(6), 1–21, doi:10.1371/journal.pone.0127563, 2015.
- Holmes, C. D., Fite, C. H., Agastra, A., Schwarz, Joshua, P., Yokelson, R. J., Bui, T. P., Kondragunta, S. and Peterson, D. A.:  
825 Critical evaluation of smoke age inferred from different methods during FIREX-AQ, in AGU Fall Meeting 2020., 2020.
- Iinuma, Y., Boge, O., Grade, R. and Herrmann, H.: Methyl-Nitrocatechols : Atmospheric Tracer Compounds for Biomass  
Burning Secondary Organic Aerosols, *Environ. Sci. Technol.*, 44, 8453–8459, 2010.
- Inciweb: 204 Cow Fire - InciWeb the Incident Information System, [online] Available from:  
https://inciweb.nwcg.gov/incident/maps/6526/ (Accessed 27 December 2020a), 2019.
- 830 Inciweb: Castle Fire - InciWeb the Incident Information System, [online] Available from:  
https://inciweb.nwcg.gov/incident/article/7048/53693/ (Accessed 27 December 2020b), 2019.
- Inciweb: Williams Flats Fire - InciWeb the Incident Information System, [online] Available from:  
https://inciweb.nwcg.gov/incident/6493/ (Accessed 27 December 2020c), 2019.
- Jaffe, D. A. and Wigder, N. L.: Ozone production from wildfires: A critical review, *Atmos. Environ.*, 51, 1–10,  
835 doi:http://dx.doi.org/10.1016/j.atmosenv.2011.11.063, 2012.
- Jaffe, D. A., O'Neill, S. M., Larkin, N. K., Holder, A. L., Peterson, D. L., Halofsky, J. E. and Rappold, A. G.: Wildfire and  
prescribed burning impacts on air quality in the United States, *J. Air Waste Manag. Assoc.*, 70(6), 583–615,  
doi:10.1080/10962247.2020.1749731, 2020.
- Jenkin, M. E., Saunders, S. M. and Pilling, M. J.: The tropospheric degradation of volatile organic compounds: a protocol for  
840 mechanism development, *Atmos. Environ.*, 31(1), 81–104, doi:10.1016/S1352-2310(96)00105-7, 1997.
- Jenkin, M. E., Saunders, S. M., Wagner, V. and Pilling, M. J.: Protocol for the development of the Master Chemical  
Mechanism, MCM v3 (Part B): Tropospheric degradation of aromatic volatile organic compounds, *Atmos. Chem. Phys.*, 3(1),  
181–193, doi:10.5194/acp-3-181-2003, 2003.
- Jenkin, M. E., Wyche, K. P., Evans, C. J., Carr, T., Monks, P. S., Alfarra, M. R., Barley, M. H., McFiggans, G. B., Young, J.  
845 C. and Rickard, A. R.: Development and chamber evaluation of the MCM v3.2 degradation scheme for  $\beta$ -caryophyllene,  
*Atmos. Chem. Phys.*, 12(11), 5275–5308, doi:10.5194/acp-12-5275-2012, 2012.
- Jenkin, M. E., Young, J. C. and Rickard, A. R.: The MCM v3.3.1 degradation scheme for isoprene, *Atmos. Chem. Phys.*,  
15(20), 11433–11459, doi:10.5194/acp-15-11433-2015, 2015.
- Keyword, M., Cope, M., Meyer, C. P. P. M., Iinuma, Y. and Emmerson, K.: When smoke comes to town: The impact of  
850 biomass burning smoke on air quality, *Atmos. Environ.*, 121, 13–21, doi:10.1016/j.atmosenv.2015.03.050, 2015.
- Kodros, J., Papanastasiou, D., Paglione, M., Masiol, M. and Squizzato, S.: The oxidizing power of the dark side : Rapid  
nocturnal aging of biomass burning as an overlooked source of oxidized organic aerosol, , 7382,  
doi:10.1073/pnas.2010365117, 2020.
- Koss, A. R., Sekimoto, K., Gilman, J. B., Selimovic, V., Coggon, M. M., Zarzana, K. J., Yuan, B., Lerner, B. M., Brown, S.  
855 S., Jimenez, J. L., Krechmer, J., Roberts, J. M., Warneke, C., Yokelson, R. J. and de Gouw, J.: Non-methane organic gas  
emissions from biomass burning: identification, quantification, and emission factors from PTR-ToF during the FIREX 2016



- laboratory experiment, *Atmos. Chem. Phys.*, 18(October), 3299–3319, doi:10.5194/acp-2017-924, 2018.
- Kupc, A., Williamson, C., Wagner, N. L., Richardson, M. and Brock, C. A.: Modification, calibration, and performance of the Ultra-High Sensitivity Aerosol Spectrometer for particle size distribution and volatility measurements during the Atmospheric Tomography Mission (ATom) airborne campaign, *Atmos. Meas. Tech.*, 11(1), 369–383, doi:10.5194/amt-11-369-2018, 2018.
- 860 LAS: Laser Aerosol Spectrometer 3340A -, [online] Available from: <https://www.tsi.com/products/particle-sizers/particle-size-spectrometers/laser-aerosol-spectrometer-3340a/> (Accessed 18 March 2021), n.d.
- Lauraguais, A., Coeur-Tourneur, C., Cassez, A., Deboudt, K., Fourmentin, M. and Choël, M.: Atmospheric reactivity of hydroxyl radicals with guaiacol (2-methoxyphenol), a biomass burning emitted compound: Secondary organic aerosol formation and gas-phase oxidation products, *Atmos. Environ.*, 86, 155–163, doi:10.1016/j.atmosenv.2013.11.074, 2014.
- 865 Lee, B. H., Lopez-Hilfiker, F. D., Mohr, C., Kurtén, T., Worsnop, D. R. and Thornton, J. A.: An iodide-adduct high-resolution time-of-flight chemical-ionization mass spectrometer: Application to atmospheric inorganic and organic compounds, *Environ. Sci. Technol.*, 48(11), 6309–6317, doi:10.1021/es500362a, 2014.
- Li, F., Zhang, X., Roy, D. P. and Kondragunta, S.: Estimation of biomass-burning emissions by fusing the fire radiative power retrievals from polar-orbiting and geostationary satellites across the conterminous United States, *Atmos. Environ.*, 211(November 2018), 274–287, doi:10.1016/j.atmosenv.2019.05.017, 2019.
- 870 Lin, P., Liu, J., Shilling, J. E., Kathmann, S. M., Laskin, J. and Laskin, A.: Molecular characterization of brown carbon (BrC) chromophores in secondary organic aerosol generated from photo-oxidation of toluene, *Phys. Chem. Chem. Phys.*, 17(36), 23312–23325, doi:10.1039/C5CP02563J, 2015.
- 875 Liu, C., Liu, J., Liu, Y., Chen, T. and He, H.: Secondary organic aerosol formation from the OH-initiated oxidation of guaiacol under different experimental conditions, *Atmos. Environ.*, 207, 30–37, doi:10.1016/j.atmosenv.2019.03.021, 2019.
- Liu, X., Zhang, Y., Huey, L. G., Yokelson, R. J., Wang, Y., Jimenez, J. L., Campuzano-Jost, P., Beyersdorf, A. J., Blake, D. R., Choi, Y., St. Clair, J. M., Crouse, J. D., Day, D. A., Diskin, G. S., Fried, A., Hall, S. R., Hanisco, T. F., King, L. E., Meinardi, S., Mikoviny, T., Palm, B. B., Peischl, J., Perring, A. E., Pollack, I. B., Ryerson, T. B., Sachse, G., Schwarz, J. P., Simpson, I. J., Tanner, D. J., Thornhill, K. L., Ullmann, K., Weber, R. J., Wennberg, P. O., Wisthaler, A., Wolfe, G. M. and Ziemba, L. D.: Agricultural fires in the southeastern U.S. during SEAC4RS: Emissions of trace gases and particles and evolution of ozone, reactive nitrogen, and organic aerosol, *J. Geophys. Res. Atmos.*, 121(12), 7383–7414, doi:10.1002/2016JD025040, 2016.
- 880 Lu, X., Zhang, L., Yue, X., Zhang, J., Jaffe, D. A., Stohl, A., Zhao, Y. and Shao, J.: Wildfire influences on the variability and trend of summer surface ozone in the mountainous western United States, *Atmos. Chem. Phys.*, 16(22), 14687–14702, doi:10.5194/acp-16-14687-2016, 2016.
- Marlon, J. R., Bartlein, P. J., Gavin, D. G., Long, C. J., Anderson, R. S., Briles, C. E., Brown, K. J., Colombaroli, D., Hallett, D. J., Power, M. J., Scharf, E. A. and Walsh, M. K.: Long-term perspective on wildfires in the western USA, *Proc. Natl. Acad. Sci. U. S. A.*, 109(9), 535–543, doi:10.1073/pnas.1112839109, 2012.
- 890 McDuffie, E. E., Fibiger, D. L., Dubé, W. P., Lopez-Hilfiker, F., Lee, B. H., Thornton, J. A., Shah, V., Jaeglé, L., Guo, H.,



- 895 Weber, R. J., Michael Reeves, J., Weinheimer, A. J., Schroder, J. C., Campuzano-Jost, P., Jimenez, J. L., Dibb, J. E., Veres, P., Ebben, C., Sparks, T. L., Wooldridge, P. J., Cohen, R. C., Hornbrook, R. S., Apel, E. C., Campos, T., Hall, S. R., Ullmann, K. and Brown, S. S.: Heterogeneous N<sub>2</sub>O<sub>5</sub> Uptake During Winter: Aircraft Measurements During the 2015 WINTER Campaign and Critical Evaluation of Current Parameterizations, *J. Geophys. Res. Atmos.*, 123(8), 4345–4372, doi:10.1002/2018JD028336, 2018.
- Meng, L., Coeur, C., Fayad, L., Houzel, N., Genevray, P., Bouzidi, H., Tomas, A. and Chen, W.: Secondary organic aerosol formation from the gas-phase reaction of guaiacol (2-methoxyphenol) with NO<sub>3</sub> radicals, *Atmos. Environ.*, 240, 117740, doi:10.1016/j.atmosenv.2020.117740, 2020.
- 900 Min, K.-E., Washenfelder, R. a., Dubé, W. P., Langford, a. O., Edwards, P. M., Zarzana, K. J., Stutz, J., Lu, K., Rohrer, F., Zhang, Y. and Brown, S. S.: A broadband cavity enhanced absorption spectrometer for aircraft measurements of glyoxal, methylglyoxal, nitrous acid, nitrogen dioxide, and water vapor, *Atmos. Meas. Tech. Discuss.*, 9(10), 423–440, doi:10.5194/amtd-8-11209-2015, 2016.
- Mohr, C., Lopez-Hilfiker, F. D., Zotter, P., Prévôit, A. S. H., Xu, L., Ng, N. L., Herndon, S. C., Williams, L. R., Franklin, J. P., Zahniser, M. S., Worsnop, D. R., Knighton, W. B., Aiken, A. C., Gorkowski, K. J., Dubey, M. K., Allan, J. D. and Thornton, 905 J. A.: Contribution of Nitrated Phenols to Wood Burning Brown Carbon Light Absorption in Detling, United Kingdom During Winter Time, *Environ. Sci. Technol.*, 47(12), 6316–6324, doi:10.1021/es400683v, 2013.
- Mondello, L., Tranchida, P. Q., Dugo, P. and Dugo, G.: Comprehensive two-dimensional gas chromatography-mass spectrometry: A review, *Mass Spectrom. Rev.*, 27(2), 101–124, doi:10.1002/mas.20158, 2008.
- 910 Moore, R. H., Wiggins, E. B., Ahern, A. T., Zimmerman, S., Jost, P. C., Robinson, C. E., Ziemba, L. D., Winstead, E. L., Anderson, B. E., Brock, C. A., Brown, M. D., Chen, G., Crosbie, E. C., Jimenez, J. L., Jordan, C. E., Lyu, M., Nault, B. A., Rothfuss, N. E., Sanchez, K. J., Schueneman, M., Shingler, T. J., Shook, M. A., Kenneth, L., Wagner, N. L. and Wang, J.: Sizing Response of the Ultra-High Sensitivity Aerosol Size Spectrometer ( UHSAS ) and Laser Aerosol Spectrometer ( LAS ) to Changes in Submicron Aerosol Composition and Refractive Index, *Atmos. Meas. Tech.*, doi:10.5194/amt-2021-21, 2021.
- 915 Nakao, S., Clark, C., Tang, P., Sato, K. and Cocker, D.: Secondary organic aerosol formation from phenolic compounds in the absence of NO<sub>x</sub>, *Atmos. Chem. Phys.*, 11(20), 10649–10660, doi:10.5194/acp-11-10649-2011, 2011.
- Neuman, J. A., Trainer, M., Brown, S. S., Min, K. E., Nowak, J. B., Parrish, D. D., Peischl, J., Pollack, I. B., Roberts, J. M., Ryerson, T. B. and Veres, P. R.: HONO emission and production determined from airborne measurements over the Southeast U.S., *J. Geophys. Res.*, 121(15), 9237–9250, doi:10.1002/2016JD025197, 2016.
- 920 NIFC: NIFC 2019 Statistics and Summary, [online] Available from: [https://www.predictiveservices.nifc.gov/intelligence/2019\\_statsumm/2019Stats&Summ.html](https://www.predictiveservices.nifc.gov/intelligence/2019_statsumm/2019Stats&Summ.html) (Accessed 8 January 2021), 2019.
- Olariu, R., Klotz, B., Barnes, I., Becker, K. and Mocanu, R.: FT – IR study of the ring-retaining products from the reaction of OH radicals with phenol , o - , m - , and p -cresol, *Atmos. Environ.*, 36(22), 3685–3697, doi:[https://doi.org/10.1016/S1352-2310\(02\)00202-9](https://doi.org/10.1016/S1352-2310(02)00202-9), 2002.



- 925 Olariu, R. I., Barnes, I., Bejan, I., Arsene, C., Vione, D., Klotz, B. and Becker, K. H.: FT-IR Product Study of the Reactions of NO<sub>3</sub> Radicals With ortho-, meta-, and para-Cresol, *Environ. Sci. Technol.*, 47(14), 7729–7738, doi:10.1021/es401096w, 2013.
- Osthoff, H. D., Sommariva, R., Baynard, T., Pettersson, A., Williams, E. J., Lerner, B. M., Roberts, J. M., Stark, H., Goldan, P. D., Kuster, W. C., Bates, T. S., Coffman, D., Ravishankara, A. R. and Brown, S. S.: Observation of daytime N<sub>2</sub>O<sub>5</sub> in the marine boundary layer during New England Air Quality Study - Intercontinental Transport and Chemical Transformation 2004, *J. Geophys. Res. Atmos.*, 111(23), doi:10.1029/2006JD007593, 2006.
- 930 Palm, B. B., Campuzano-Jost, P., Day, D. A., Ortega, A. M., Fry, J. L., Brown, S. S., Zarzana, K. J., Dube, W., Wagner, N. L., Draper, D. C., Kaser, L., Jud, W., Karl, T., Hansel, A., Gutiérrez-Montes, C. and Jimenez, J. L.: Secondary organic aerosol formation from in situ OH, O<sub>3</sub>, and NO<sub>3</sub> oxidation of ambient forest air in an oxidation flow reactor, *Atmos. Chem. Phys.*, 17(8), 5331–5354, doi:10.5194/acp-17-5331-2017, 2017.
- 935 Palm, B. B., Peng, Q., Fredrickson, C. D., Lee, B. H., Garofalo, L. A., Pothier, M. A., Kreidenweis, S. M., Farmer, D. K., Pokhrel, R. P., Shen, Y., Murphy, S. M., Permar, W., Hu, L., Campos, T. L., Hall, S. R., Ullmann, K., Zhang, X., Flocke, F., Fischer, E. V. and Thornton, J. A.: Quantification of organic aerosol and brown carbon evolution in fresh wildfire plumes, *Proc. Natl. Acad. Sci. U. S. A.*, 117(47), 29469–29477, doi:10.1073/pnas.2012218117, 2020.
- 940 Parks, S. A., Miller, C., Parisien, M. A., Holsinger, L. M., Dobrowski, S. Z. and Abatzoglou, J.: Wildland fire deficit and surplus in the western United States, 1984–2012, *Ecosphere*, 6(12), 1–13, doi:10.1890/ES15-00294.1, 2015.
- Peng, Q., Palm, B. B., Melander, K. E., Lee, B. H., Hall, S. R., Ullmann, K., Campos, T., Weinheimer, A. J., Apel, E. C., Hornbrook, R. S., Hills, A. J., Montzka, D. D., Flocke, F., Hu, L., Permar, W., Wielgasz, C., Lindaas, J., Pollack, I. B., Fischer, E. V., Bertram, T. H. and Thornton, J. A.: HONO Emissions from Western U.S. Wildfires Provide Dominant Radical Source in Fresh Wildfire Smoke, *Environ. Sci. Technol.*, 54(10), 5954–5963, doi:10.1021/acs.est.0c00126, 2020.
- 945 Phuleria, H. C., Fine, P. M., Zhu, Y. and Sioutas, C.: Air quality impacts of the October 2003 Southern California wildfires, *J. Geophys. Res. Atmos.*, 110(7), 1–11, doi:10.1029/2004JD004626, 2005.
- Pollack, I. B., Lerner, B. M. and Ryerson, T. B.: Evaluation of ultraviolet light-emitting diodes for detection of atmospheric NO<sub>2</sub> by photolysis - Chemiluminescence, *J. Atmos. Chem.*, 65(2–3), 111–125, doi:10.1007/s10874-011-9184-3, 2010.
- 950 Ridley, B. A., Grahek, F. E. and Walega, J. G.: A Small High-Sensitivity, Medium-Response Ozone Detector Suitable for Measurements from Light Aircraft, *J. Atmos. Ocean. Technol.*, 9(2), 142–148, doi:10.1175/1520-0426(1992)009<0142:ASHSMR>2.0.CO;2, 1992.
- Ro Lee, Y., Ji, Y., Tanner, D. J. and Gregory Huey, L.: A low-activity ion source for measurement of atmospheric gases by chemical ionization mass spectrometry, *Atmos. Meas. Tech.*, 13(5), 2473–2480, doi:10.5194/amt-13-2473-2020, 2020.
- 955 Roberts, J. M., Stockwell, C. E., Yokelson, R. J., De Gouw, J., Liu, Y., Selimovic, V., Koss, A. R., Sekimoto, K., Coggon, M. M., Yuan, B., Zarzana, K. J., Brown, S. S., Santin, C., Doerr, S. H. and Warneke, C.: The nitrogen budget of laboratory-simulated western US wildfires during the FIREX 2016 Fire Lab study, *Atmos. Chem. Phys.*, 20(14), 8807–8826, doi:10.5194/acp-20-8807-2020, 2020.



- Rollins, A. W., Rickly, P. S., Gao, R. S., Ryerson, T. B., Brown, S. S., Peischl, J. and Bourgeois, I.: Single-photon laser-  
960 induced fluorescence detection of nitric oxide at sub-parts-per-trillion mixing ratios, *Atmos. Meas. Tech.*, 13(5), 2425–2439,  
doi:10.5194/amt-13-2425-2020, 2020.
- Sachse, G. W., Collins Jr, J. E., Hill, G. F., Wade, L. O., Lewis, B. G. and Ritter, J. A.: Airborne tunable diode laser sensor for  
high-precision concentration and flux measurements of carbon monoxide and methane, *Proc. SPIE*, 1433, 157–166,  
doi:10.1117/12.46162, 1991.
- 965 Sangwan, M. and Zhu, L.: Absorption cross sections of 2-Nitrophenol in the 295–400 nm region and photolysis of  
2-Nitrophenol at 308 and 351 nm, *J. Phys. Chem. A*, 120(50), 9958–9967, doi:10.1021/acs.jpca.6b08961, 2016.
- Sangwan, M. and Zhu, L.: Role of Methyl-2-nitrophenol Photolysis as a Potential Source of OH Radicals in the Polluted  
Atmosphere: Implications from Laboratory Investigation, *J. Phys. Chem. A*, 122(7), 1861–1872,  
doi:10.1021/acs.jpca.7b11235, 2018.
- 970 Saunders, S. M., Pascoe, S., Johnson, A. P., Pilling, M. J. and Jenkin, M. E.: Development and preliminary test results of an  
expert system for the automatic generation of tropospheric VOC degradation mechanisms, *Atmos. Environ.*, 37(13), 1723–  
1735, doi:10.1016/S1352-2310(03)00072-4, 2003.
- Schwantes, R. H., Schilling, K. A., McVay, R. C., Lignell, H., Coggon, M. M., Zhang, X., Wennberg, P. O. and Seinfeld, J.  
H.: Formation of highly oxygenated low-volatility products from cresol oxidation, *Atmos. Chem. Phys.*, 17(5), 3453–3474,  
975 doi:10.5194/acp-17-3453-2017, 2017.
- Selimovic, V., Yokelson, R. J., McMeeking, G. R. and Coefield, S.: Aerosol Mass and Optical Properties, Smoke Influence  
on O<sub>3</sub>, and High NO<sub>3</sub> Production Rates in a Western U.S. City Impacted by Wildfires, *J. Geophys. Res. Atmos.*, 125(16), 1–  
22, doi:10.1029/2020JD032791, 2020.
- Shetter, R. E. and Müller, M.: Photolysis frequency measurements using actinic flux spectroradiometry during the PEM-  
980 Tropics mission: Instrumentation description and some results, *J. Geophys. Res. Atmos.*, 104(D5), 5647–5661,  
doi:10.1029/98JD01381, 1999.
- Silvern, R. F., Jacob, D. J., Mickley, L. J., Sulprizio, M. P., Travis, K. R., Marais, E. A., Cohen, R. C., Laughner, J. L., Choi,  
S., Joiner, J. and Lamsal, L. N.: Using satellite observations of tropospheric NO<sub>2</sub> columns to infer long-term trends in US NO<sub>x</sub>  
emissions: The importance of accounting for the free tropospheric NO<sub>2</sub> background, *Atmos. Chem. Phys.*, 19(13), 8863–8878,  
985 doi:10.5194/acp-19-8863-2019, 2019.
- SMPS: Scanning Mobility Particle Sizer Spectrometer 3936 -, [online] Available from: <https://tsi.com/discontinued-products/scanning-mobility-particle-sizer-spectrometer-3936/> (Accessed 18 March 2021), n.d.
- Sparks, T. L., Ebben, C. J., Wooldridge, P. J., Lopez-Hilfiker, F. D., Lee, B. H., Thornton, J. A., McDuffie, E. E., Fibiger, D.  
L., Brown, S. S., Montzka, D. D., Weinheimer, A. J., Schroder, J. C., Campuzano-Jost, P., Jimenez, J. L. and Cohen, R. C.:  
990 Comparison of Airborne Reactive Nitrogen Measurements During WINTER, *J. Geophys. Res. Atmos.*, 124(19), 10483–10502,  
doi:10.1029/2019JD030700, 2019.
- Stedman, D. H., Daby, E. E., Stuhl, F. and Niki, H.: Analysis of ozone and nitric oxide by a chemiluminescent method in



- laboratory and atmospheric studies of photochemical smog, *J. Air Pollut. Control Assoc.*, 22(4), 260–263, doi:10.1080/00022470.1972.10469635, 1972.
- 995 Veres, P. R., Andrew Neuman, J., Bertram, T. H., Assaf, E., Wolfe, G. M., Williamson, C. J., Weinzierl, B., Tilmes, S., Thompson, C. R., Thames, A. B., Schroder, J. C., Saiz-Lopez, A., Rollins, A. W., Roberts, J. M., Price, D., Peischl, J., Nault, B. A., Møller, K. H., Miller, D. O., Meinardi, S., Li, Q., Lamarque, J. F., Kupc, A., Kjaergaard, H. G., Kinnison, D., Jimenez, J. L., Jernigan, C. M., Hornbrook, R. S., Hills, A., Dollner, M., Day, D. A., Cuevas, C. A., Campuzano-Jost, P., Burkholder, J., Paul Bui, T., Brune, W. H., Brown, S. S., Brock, C. A., Bourgeois, I., Blake, D. R., Apel, E. C. and Ryerson, T. B.: Global  
1000 airborne sampling reveals a previously unobserved dimethyl sulfide oxidation mechanism in the marine atmosphere, *Proc. Natl. Acad. Sci. U. S. A.*, 117(9), 4505–4510, doi:10.1073/pnas.1919344117, 2020.
- Wagner, N. L., Riedel, T. P., Young, C. J., Bahreini, R., Brock, C. A., Dubé, W. P., Kim, S., Middlebrook, A. M., Öztürk, F., Roberts, J. M., Russo, R., Sive, B., Swarthout, R., Thornton, J. A., VandenBoer, T. C., Zhou, Y. and Brown, S. S.: N<sub>2</sub>O<sub>5</sub> uptake coefficients and nocturnal NO<sub>2</sub> removal rates determined from ambient wintertime measurements, *J. Geophys. Res.*  
1005 *Atmos.*, 118(16), 9331–9350, doi:10.1002/jgrd.50653, 2013.
- Wang, S. and Li, H.: NO<sub>3</sub>-Initiated Gas-Phase Formation of Nitrated Phenolic Compounds in Polluted Atmosphere, *Environ. Sci. Technol.*, (3), doi:10.1021/acs.est.0c08041, 2021.
- Warneke, C., De Gouw, J. A., Holloway, J. S., Peischl, J., Ryerson, T. B., Atlas, E., Blake, D., Trainer, M. and Parrish, D. D.: Multiyear trends in volatile organic compounds in Los Angeles, California: Five decades of decreasing emissions, *J. Geophys.*  
1010 *Res. Atmos.*, 117(17), 1–10, doi:10.1029/2012JD017899, 2012.
- Warneke, C., Trainer, M., De Gouw, J. A., Parrish, D. D., Fahey, D. W., Ravishankara, A. R., Middlebrook, A. M., Brock, C. A., Roberts, J. M., Brown, S. S., Neuman, J. A., Lerner, B. M., Lack, D., Law, D., Hübler, G., Pollack, I., Sjostedt, S., Ryerson, T. B., Gilman, J. B., Liao, J., Holloway, J., Peischl, J., Nowak, J. B., Aikin, K. C., Min, K. E., Washenfelder, R. A., Graus, M. G., Richardson, M., Markovic, M. Z., Wagner, N. L., Welti, A., Veres, P. R., Edwards, P., Schwarz, J. P., Gordon, T., Dube,  
1015 W. P., McKeen, S. A., Brioude, J., Ahmadov, R., Bougiatioti, A., Lin, J. J., Nenes, A., Wolfe, G. M., Hanisco, T. F., Lee, B. H., Lopez-Hilfiker, F. D., Thornton, J. A., Keutsch, F. N., Kaiser, J., Mao, J. and Hatch, C. D.: Instrumentation and measurement strategy for the NOAA SENEX aircraft campaign as part of the Southeast Atmosphere Study 2013, *Atmos. Meas. Tech.*, 9(7), 3063–3093, doi:10.5194/amt-9-3063-2016, 2016.
- Wayne, R. ., Barnes, I., Biggs, P., Burrows, J. ., Canosa-Mas, C. ., Hjorth, J., Le Bras, G., Moortgat, G. ., Perner, D., Poulet,  
1020 G., Restelli, G. and Sidebottom, H.: The nitrate radical: Physics, chemistry, and the atmosphere, *Atmos. Environ. Part A. Gen. Top.*, 25(1), 1–203, doi:10.1016/0960-1686(91)90192-A, 1991.
- Westerling, A. L., Hidalgo, H. G., Cayan, D. R. and Swetnam, T. W.: Warming and Earlier Spring Increase Western U.S. Forest Wildfire Activity, *Science* (80-. ), 313(5789), 940–943 [online] Available from: <http://www.sciencemag.org/content/313/5789/940.abstract>, 2006.
- 1025 Westerling, A. L. R.: Increasing western US forest wildfire activity: Sensitivity to changes in the timing of spring, *Philos. Trans. R. Soc. B Biol. Sci.*, 371(1696), doi:10.1098/rstb.2015.0178, 2016.



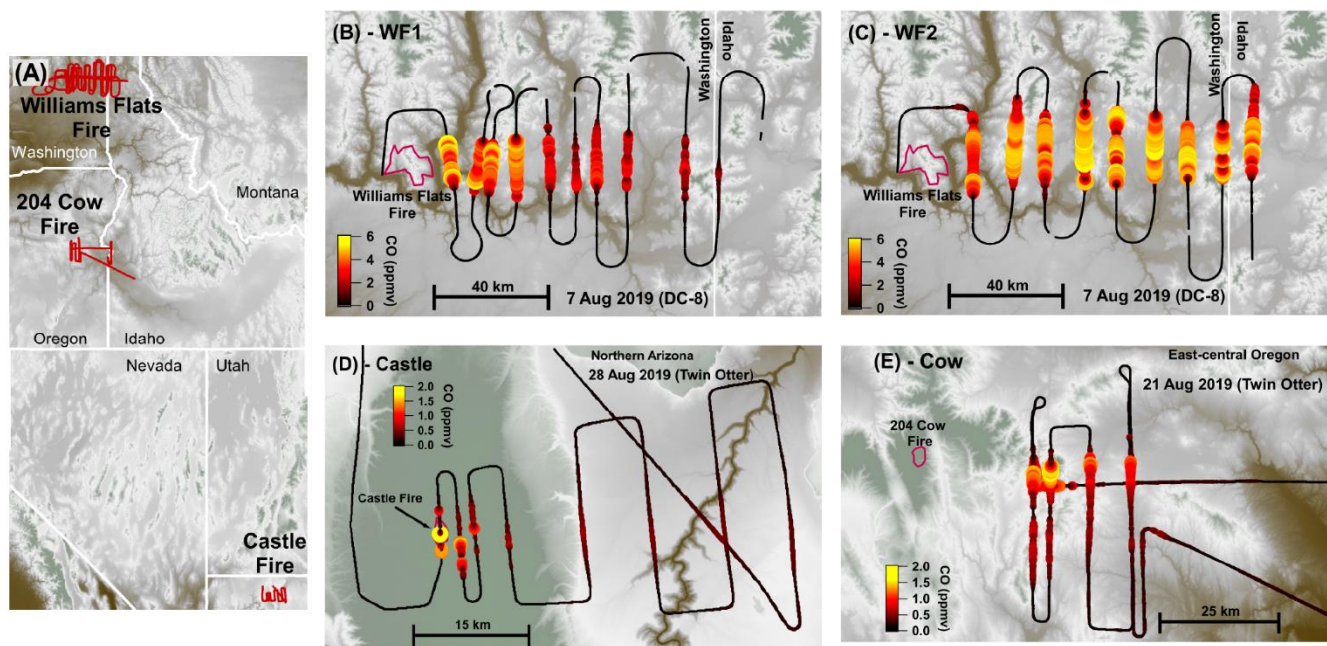
- Williams, A. P., Abatzoglou, J. T., Gershunov, A., Guzman-Morales, J., Bishop, D. A., Balch, J. K. and Lettenmaier, D. P.: Observed Impacts of Anthropogenic Climate Change on Wildfire in California, *Earth's Futur.*, 7(8), 892–910, doi:10.1029/2019EF001210, 2019.
- 1030 Wolfe, G. M., Marvin, M. R., Roberts, S. J., Travis, K. R. and Liao, J.: The framework for 0-D atmospheric modeling (F0AM) v3.1, *Geosci. Model Dev.*, 9(9), 3309–3319, doi:10.5194/gmd-9-3309-2016, 2016.
- Xie, M., Chen, X., Hays, M. D., Lewandowski, M., Offenberg, J., Kleindienst, T. E. and Holder, A. L.: Light Absorption of Secondary Organic Aerosol: Composition and Contribution of Nitroaromatic Compounds, *Environ. Sci. Technol.*, 51(20), 11607–11616, doi:10.1021/acs.est.7b03263, 2017.
- 1035 Xing, J., Mathur, R., Pleim, J., Hogrefe, C., Gan, C. M., Wong, D. C., Wei, C., Gilliam, R. and Pouliot, G.: Observations and modeling of air quality trends over 1990–2010 across the Northern Hemisphere: China, the United States and Europe, *Atmos. Chem. Phys.*, 15(5), 2723–2747, doi:10.5194/acp-15-2723-2015, 2015.
- Yang, Y., Shao, M., Wang, X., Nölscher, A. C., Kessel, S., Guenther, A. and Williams, J.: Towards a quantitative understanding of total OH reactivity: A review, *Atmos. Environ.*, 134(2), 147–161, doi:10.1016/j.atmosenv.2016.03.010, 1040 2016.
- Yang, Y., Wang, Y., Zhou, P., Yao, D., Ji, D., Sun, J., Wang, Y., Zhao, S., Huang, W., Yang, S., Chen, D., Gao, W., Liu, Z., Hu, B., Zhang, R., Zeng, L., Ge, M., Petäjä, T., Kerminen, V. M., Kulmala, M. and Wang, Y.: Atmospheric reactivity and oxidation capacity during summer at a suburban site between Beijing and Tianjin, *Atmos. Chem. Phys.*, 20(13), 8181–8200, doi:10.5194/acp-20-8181-2020, 2020.
- 1045 Yokelson, R. J., Andreae, M. O. and Akagi, S. K.: Pitfalls with the use of enhancement ratios or normalized excess mixing ratios measured in plumes to characterize pollution sources and aging, *Atmos. Meas. Tech.*, 6(8), 2155–2158, doi:10.5194/amt-6-2155-2013, 2013.
- El Zein, A., Coeur, C., Obeid, E., Lauraguais, A. and Fagniez, T.: Reaction Kinetics of Catechol (1,2-Benzenediol) and Guaiacol (2-Methoxyphenol) with Ozone, *J. Phys. Chem. A*, 119(26), 6759–6765, doi:10.1021/acs.jpca.5b00174, 2015.
- 1050



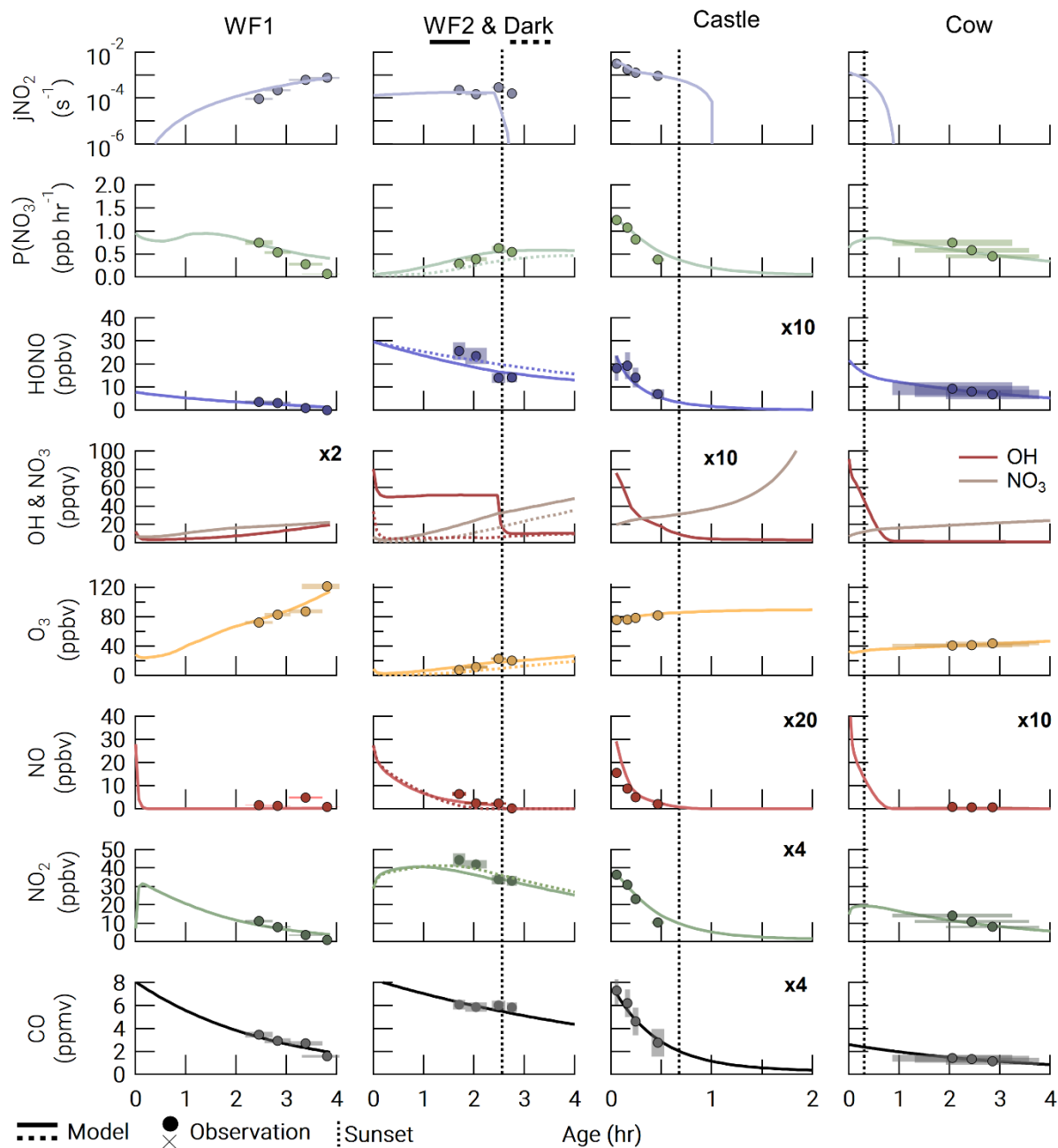
### Figures & Tables

Fire name	County/State	Latitude	Longitude	Date sampled	Time sampled	Aircraft	Fuel
Williams Flats	Ferry/Washington	47.9392	-118.6183	Aug 07	16:30–17:45 PDT & 18:00–19:30 PDT	DC-8	Short grass, ponderosa timber
Castle	Coconino/Arizona	36.5312	-112.2281	Aug 21	18:00–19:15 MST	Twin Otter	Mixed conifer
204 Cow	Grant/Oregon	44.2851	-118.4598	Aug 28	20:00–22:00 PDT	Twin Otter	Primarily lodgepole pine with conifer

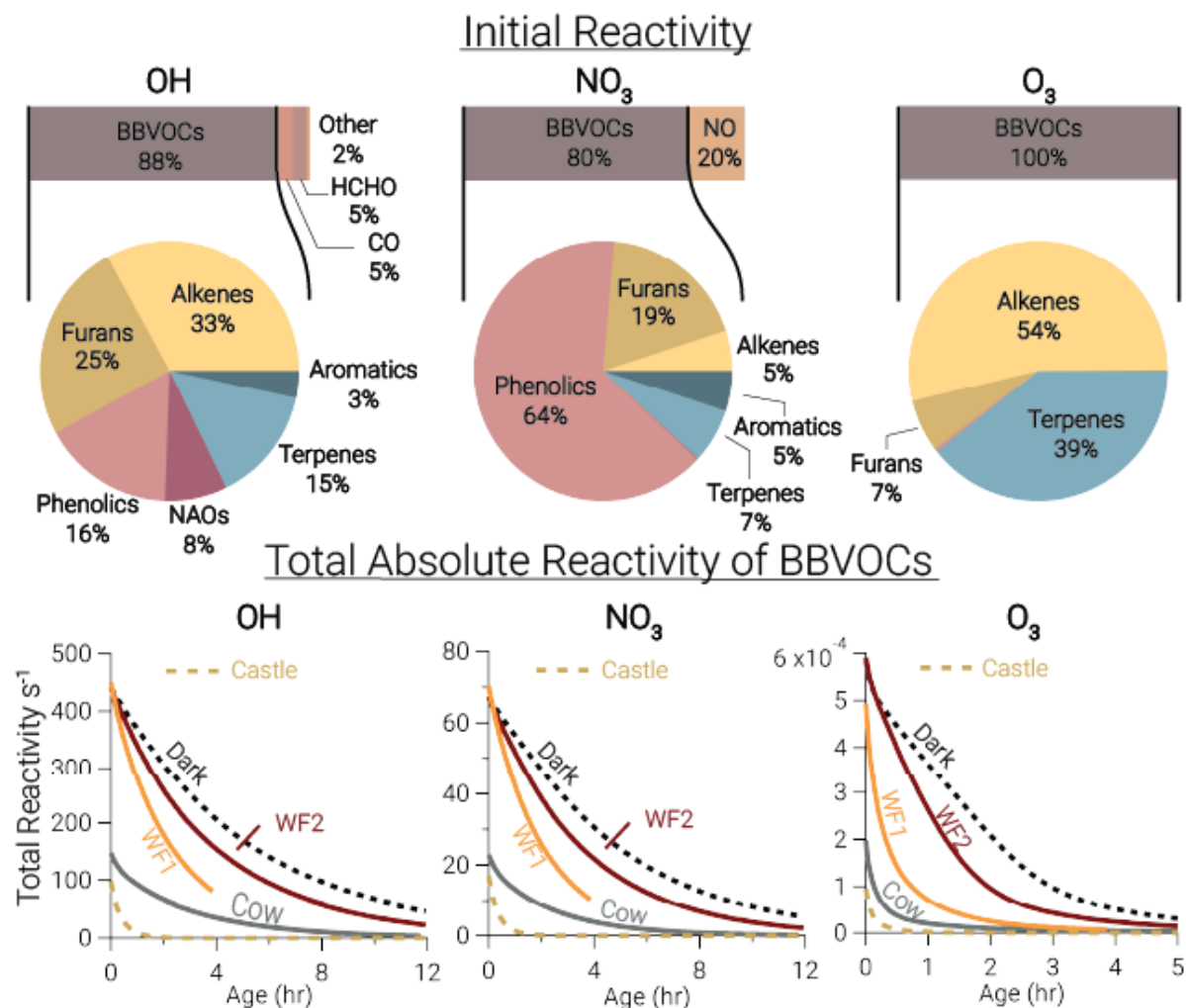
1055 **Table 1: Details of fires studied.**



1060 **Figure 1: Flight maps colored by elevation. Overview Map (A) showing flight tracks (red) with detailed flight maps of the WF1 transects (B), WF2 transects (C), Castle transects (D), and 204 Cow transects (E). Panels B–E are colored and sized by CO. Fire boundaries are approximate and indicated by red outlines. The flight path is shown in black colored and sized by CO.**



1065 **Figure 2: Observations (closed circles) and model output (lines) for all model runs. The Dark run is shown as a dashed line in the WF2 column. The time of sunset (defined as when the solar zenith angle reaches 90°) is indicated by a vertical dashed line. Observation errors (y error: variability in the observation at plume-center and instrument uncertainty added in quadrature, x error: uncertainty in plume age determination) are shown as shaded xy boxes.**



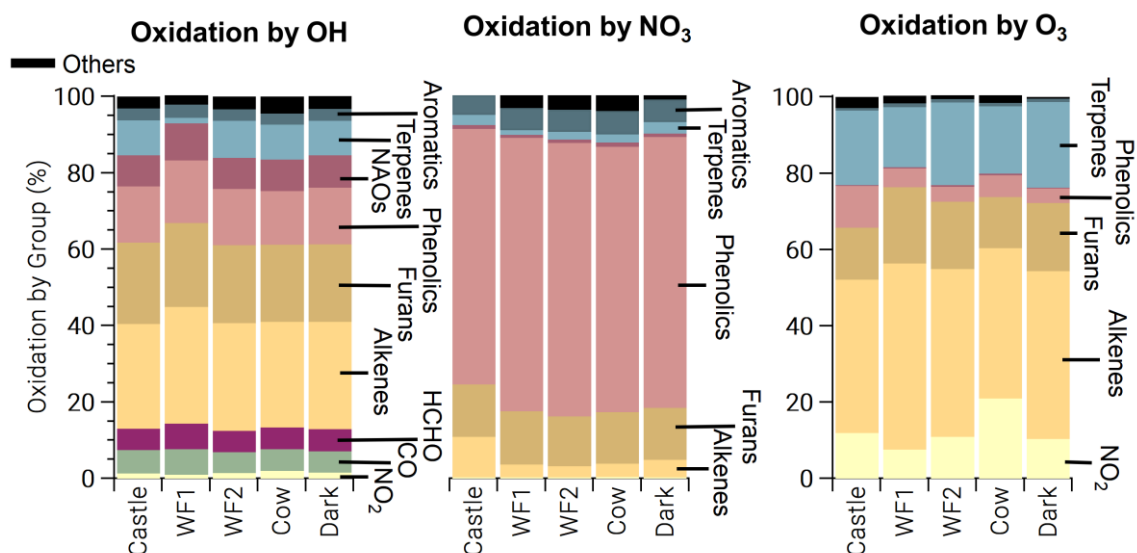
1070

**Figure 3:** Bars: Average (of all model runs) initial relative instantaneous reactivity for all compounds in our model showing that initial reactivity of BBVOCs outweighs all other compounds for all oxidants. Pies: Initial relative reactivity of BBVOCs showing that OH reactivity is controlled by many BBVOC groups, NO<sub>3</sub> reactivity by phenolics, and O<sub>3</sub> reactivity by alkenes and terpenes. Time series: Absolute reactivity of for all model runs showing that reactivity decays at different rates for each model run, and that OH and NO<sub>3</sub> reactivity decay is similar.

1075

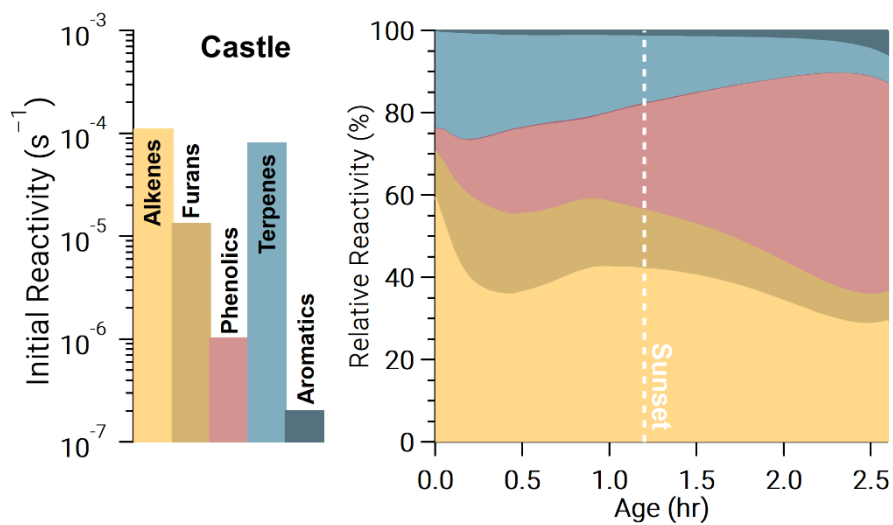


1080

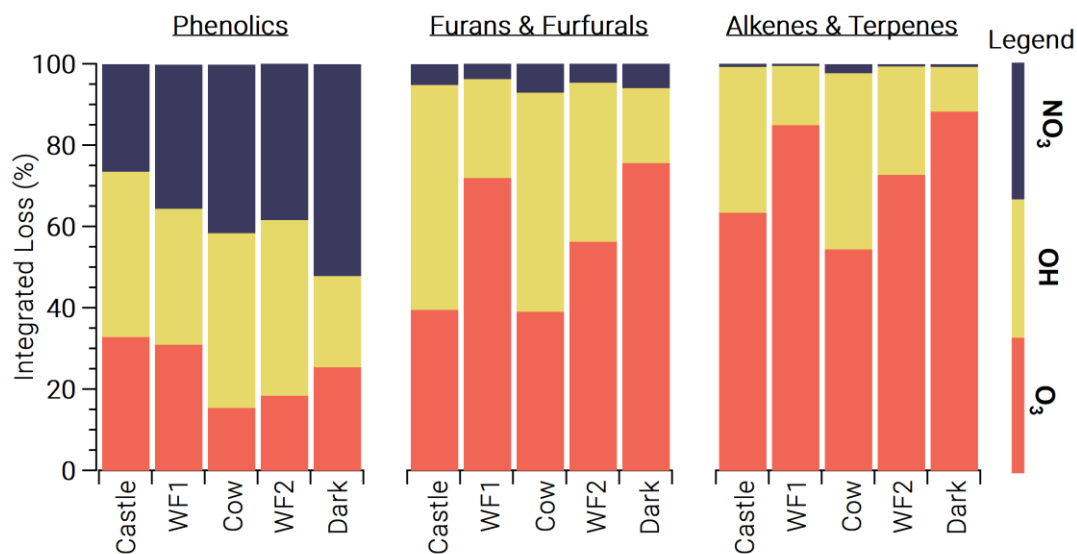


1085

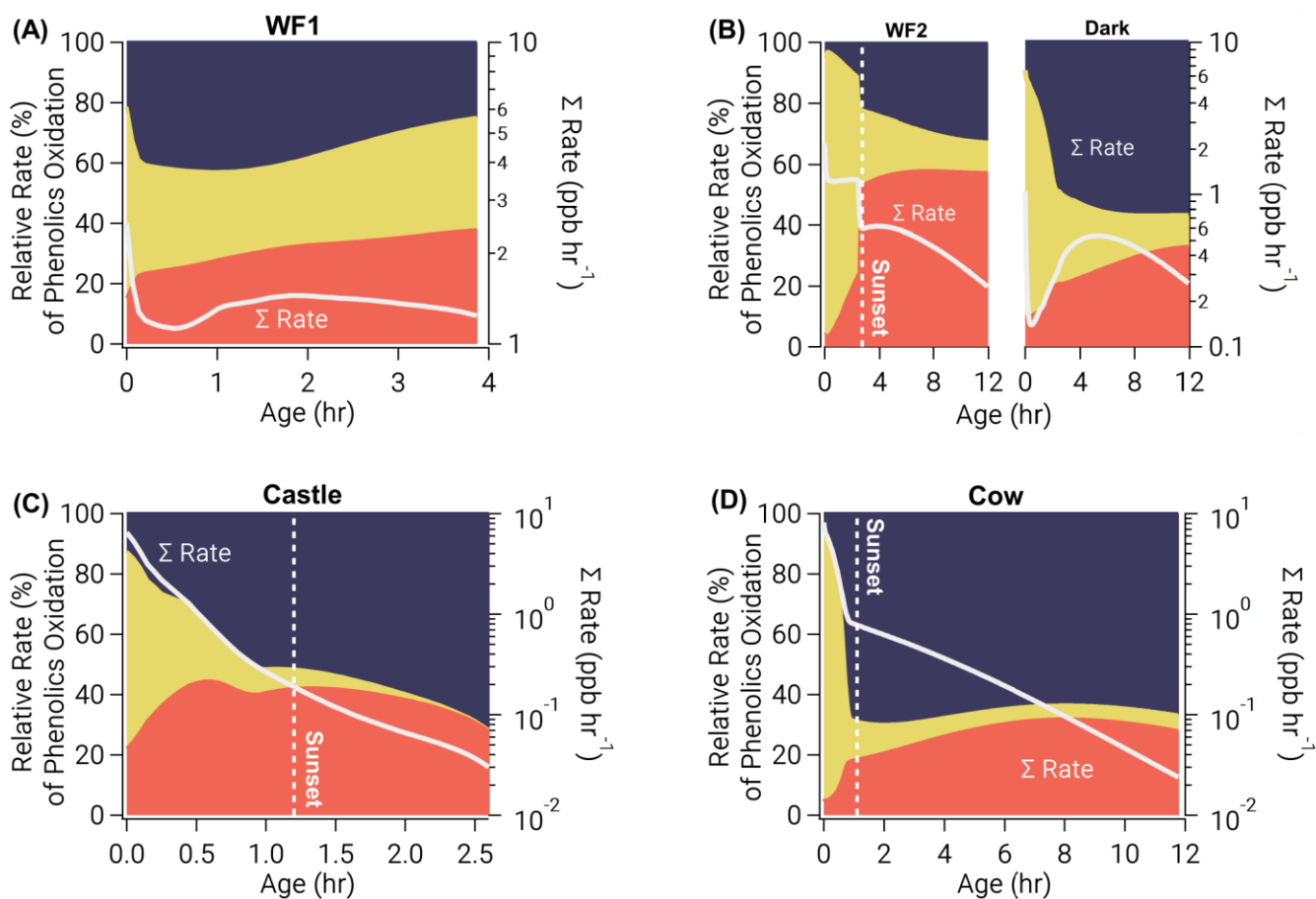
**Figure 4: Integrated oxidation rate, or oxidation budgets, of BBVOCs by OH (left), NO<sub>3</sub> (center), and O<sub>3</sub> (right) on a relative scale for all five model runs. Oxidation by OH is spread across many BBVOC groups (where NAOs are non-aromatic oxygenates), similar to initial reactivity, but also HCHO, CO, and NO<sub>2</sub>. Oxidation by NO<sub>3</sub> is dominated by phenolics, but by a greater fraction than initial reactivity suggests. Oxidation by O<sub>3</sub> is shown without NO and is dominated by alkenes and terpenes as expected from initial reactivity, but unlike initial reactivity it includes large contributions from phenolics and NO<sub>2</sub> (resulting in NO<sub>3</sub> production).**



1090 **Figure 5: Ozone reactivity from the Castle model run in the form of absolute initial reactivity (bars, log scale) and relative BBVOC reactivity as a function of plume age (stacked, linear scale). As the plume ages, O<sub>3</sub> reactivity toward each BBVOC group changes significantly.**



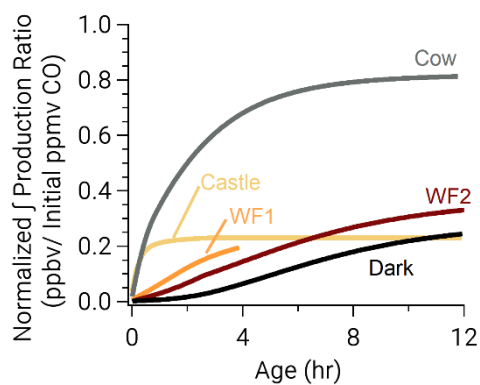
1095 **Figure 6: Integrated loss of phenolics (left), furans & furfurals (middle) and alkenes & terpenes (right) reacting with NO<sub>3</sub> (blue), OH (yellow) and O<sub>3</sub> (orange). The model runs are ordered from left to right by decreasing integrated jNO<sub>2</sub>. Generally, furan/furfurals and alkenes/terpenes are oxidized primarily by O<sub>3</sub> and OH. In contrast, phenolic oxidation is split across all oxidants.**



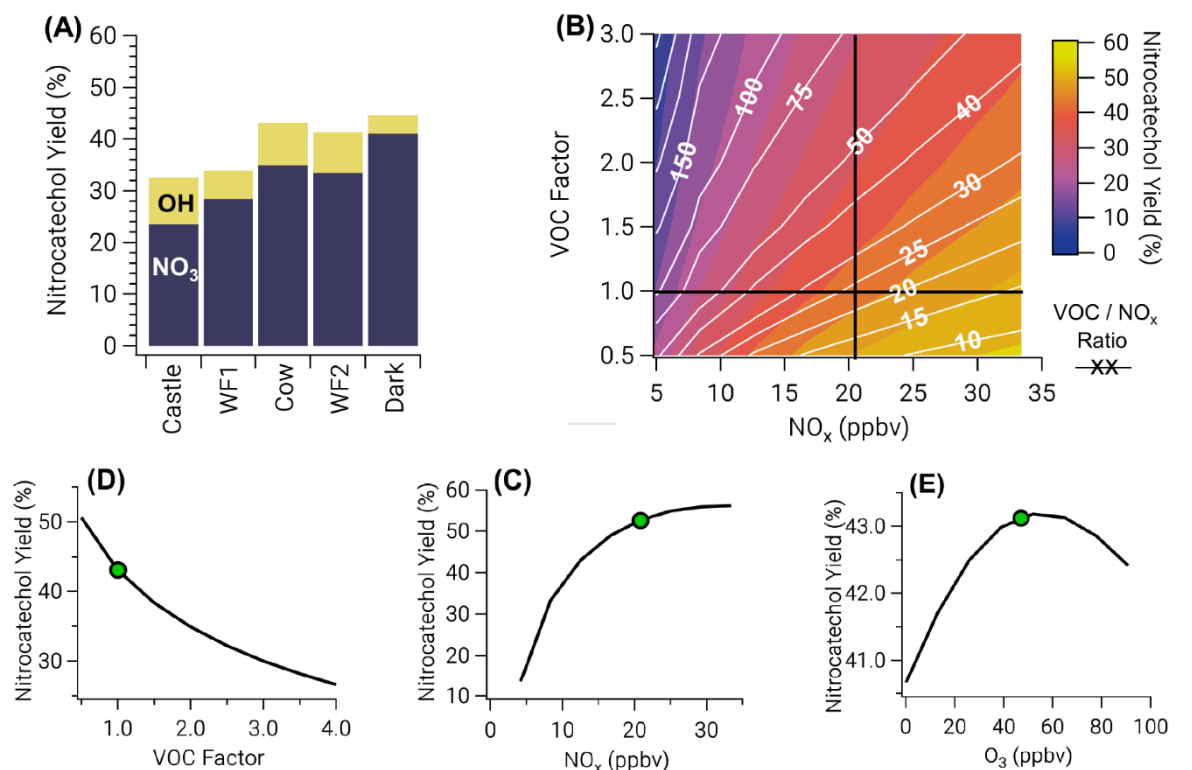
1100

**Figure 7:** Relative oxidation rate (left axis) of phenolics by  $\text{NO}_3$  (blue, top),  $\text{OH}$  (yellow, middle), and  $\text{O}_3$  (orange, bottom) for all model runs as a function of plume age. Right axis shows absolute total reactivity (white line) on a log scale. Phenolic oxidation is controlled by  $\text{OH}$  at emission, but eventually transitions to  $\text{NO}_3$  oxidation before sunset in the WF1, Castle and Cow model runs, or after sunset in the WF2 model run. Even without photolysis,  $\text{OH}$  oxidation dominates phenolic oxidation early in the Dark model run.

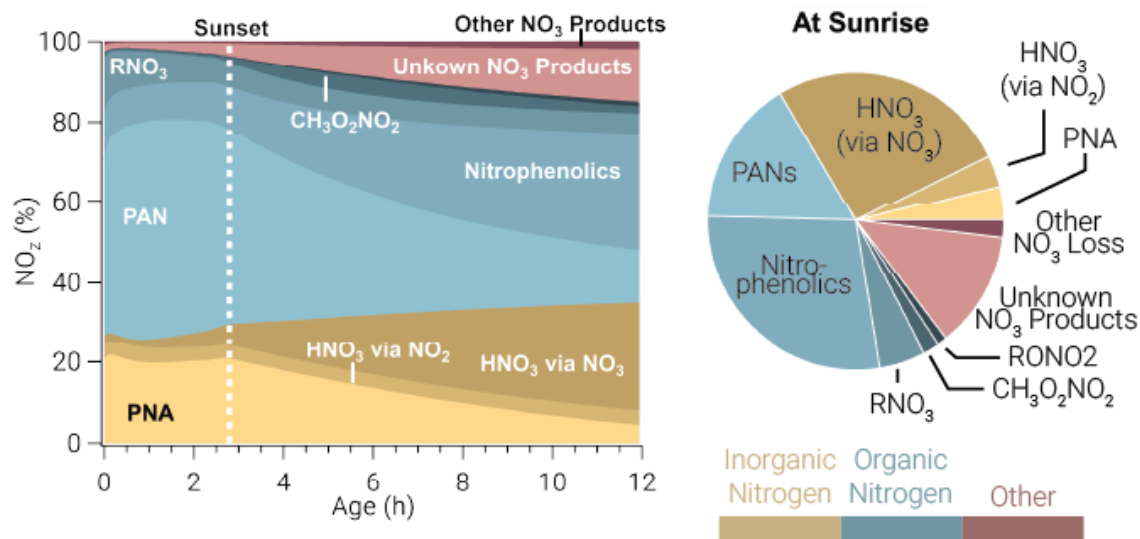
1105



1110 **Figure 8: Integrated nitrophenolic production normalized to initial CO to compare nitrophenolic production across varying amounts of initial emissions. The simulated Castle and Cow plumes form nitrophenolics quickly. Even so, the Castle plume forms less nitrophenolics than other runs.**

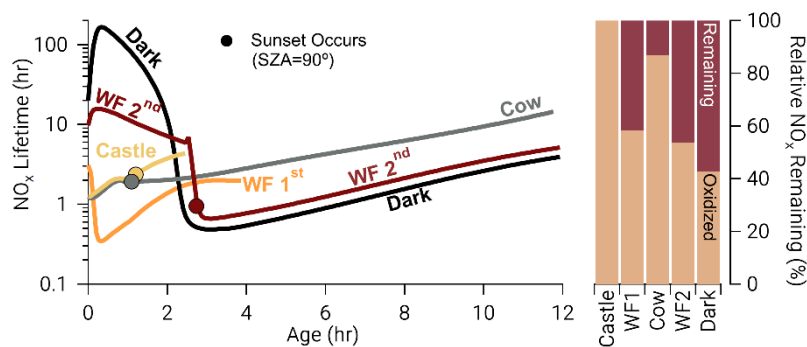


1115 **Figure 9:** Panel A: nitrocatechol yield for all model runs colored by the fraction of nitrocatechol formed from  $\text{NO}_3$  and OH oxidation  
of catechol. Panels B–E are shown for the Cow model run, which is representative of all other runs. B: two overlaid contour plots of  
VOC/ $\text{NO}_x$  ratio (white lines and white text) and nitrocatechol yield (color scale), with black cross sections that intersect at the  
observed Cow conditions. C: a cross section of B for nitrocatechol yield as a function of  $\text{NO}_x$  (horizontal black line). D: a cross section  
of B for nitrocatechol yield as a function of VOC factor, a multiple of the initial VOC emissions (vertical black line). E: nitrocatechol  
1120 yield as a function of initial  $\text{O}_3$ . Green dots in C–E indicate observed conditions used for the model run. Nitrocatechol is primarily  
formed from  $\text{NO}_3$  and the yield increases with increasing  $\text{NO}_x$ , but decreases with increasing BBVOC and BBVOC/ $\text{NO}_x$  ration.  
Ozone has little effect on nitrocatechol yield.



1125 **Figure 10: Relative integrated  $\text{NO}_x$  reservoirs and sinks for the WF2 model run as a function of plume age (left) and at sunrise (right). This result is the average between a WF2 model run constrained and unconstrained to PAN observations as explained in the main text. Gold colors indicate inorganic nitrogen, blue colors indicate organic nitrogen, and red colors indicate other forms of  $\text{NO}_x$ . In this analysis we consider HONO to be a member of  $\text{NO}_x$ , rather than  $\text{NO}_z$ . PAN and PNA dominate  $\text{NO}_2$  during the daytime, but after sunset these decompose to provide  $\text{NO}_2$  that is subsequently lost to nitrophenolics and other  $\text{NO}_3$  products overnight.**

1130



1135

**Figure 11: Time series: NO<sub>x</sub> lifetime in hours on a log scale for all model runs where closed circles indicate the time of sunset (solar zenith angle = 90°). Bars: the relative NO<sub>x</sub> remaining calculated as the fraction of NO<sub>x</sub> remaining at the end of our model divided by the amount of NO<sub>x</sub> that was reacted, excluding dilution. After the depletion of NO, NO<sub>x</sub> chemistry changes dramatically in the WF2 and Dark model runs, reducing NO<sub>x</sub> lifetime rapidly. A significant amount of NO<sub>x</sub> remains in the WF2 and Dark model runs at sunrise, providing potential for significant morning chemistry to occur.**